
Magnetic Fields in Diffuse H I and Molecular Clouds

Carl Heiles¹ and Richard Crutcher²

¹ Astronomy Department, University of California, Berkeley
cheiles@astron.berkeley.edu

² Astronomy Department, University of Illinois
crutcher@uiuc.edu

1 Introduction

The diffuse interstellar H I is the matrix within which many molecular clouds reside and the medium that soaks up the energy injected by sources such as supernovae and stellar winds. This energy stimulates turbulence in the H I, which cascades up the turbulent wavenumber spectrum. The spectral wavelengths extend all the way down to scales most easily quoted in Astronomical Units. H I and molecular clouds enjoy a synergistic relationship, with turbulent energy, angular momentum, magnetic fields, and matter flowing across the boundaries in both directions. The molecular clouds form stars, which in turn act as energy sources to round the circle and make star formation a feedback process.

Fortunately for us who study magnetic fields, the neutral medium isn't really neutral and, as a consequence, flux freezing applies. In diffuse H I the minimum free electron fraction is, at minimum, equal to that of heavy elements that have ionization potential less than that of H I ($\gtrsim 10^{-4}$) because even in the dark reaches of space there are plenty of starlight photons available to keep any such element ionized. As a crude approximation we can model a piece of the interstellar gas as a giant inductor, for which the timescale τ for decay of a current (and its associated magnetic field) is the inductance divided by the resistance; this, in turn, goes as $\tau \propto L^2/\eta$, where L is the length scale and η the resistivity. Even with the low fractional ionization, L dominates and timescales for decay are always long in diffuse H I. In dense molecular clouds starlight is excluded and the free electrons come from cosmic-ray ionization of H; the fractional ionization is small enough that slow leakage of frozen magnetic flux allows the clouds to gradually evolve.

With flux freezing, the magnetic field becomes one of the four most important forces on the diffuse gas. The others are gas pressure, cosmic-ray pressure, and gravity. Gravity dominates on the largest scales, e.g. by keeping the gas pulled down as part of the Galactic plane; it also dominates during

star formation, of course. On all other scales the gas responds only to the three pressure forces. The gas and cosmic rays are connected by the field, so they form a coupled system. The field is a – perhaps *the* – major player.

One determines the field strength in the diffuse interstellar gas in several ways. Each method has its own idiosyncrasies and provides values that are biased either up or down. Beck et al. (2003) is *required reading* to understand these biases. Synchrotron emissivity provides a volume average of $\langle B^x \rangle^{1/x}$, where $1.9 \lesssim x \lesssim 3.9$ depending on whether one assumes the electron cosmic-ray spectrum or energy equipartition (Beck 2001). Comparing pulsar rotation and dispersion measures provides a field strength in the diffuse Warm Ionized Medium (WIM). Zeeman splitting provides the field strength in the H I.

Combining these estimates gives a typical magnetic field strength $\sim 6 \pm 2 \mu\text{G}$ (Beck 2001), which is equivalent to a gas pressure $\tilde{P} \equiv P/k \sim 10400 \text{ cm}^{-3} \text{ K}$. This is about three times the typical ISM thermal gas pressure of $\sim 3000 \text{ cm}^{-3} \text{ K}$ (Jenkins & Tripp 2001, Wolfire et al. 2003), and is comparable to the other important interstellar energy densities, namely turbulence and cosmic rays. These pressures must add to provide hydrostatic support for the gas layer, estimated to be $P_{\text{tot}} \approx 28000 \text{ cm}^{-3} \text{ K}$ at $z = 0$ (Boulares & Cox 1990). Clearly, thermal pressure is a minority player; turbulence, cosmic rays, and the magnetic field dominate. One cannot hope to understand the interstellar medium without understanding the role of the magnetic field. Moreover, the crucial star formation feedback process is regulated, or stimulated, or at least greatly affected, by the magnetic field.

Magnetism makes its effects very clear in supernova shocks. These shocks compress both the gas and the field. As the gas cools behind the shock, it does so at roughly constant pressure, so its density increases. Concomitantly, the field strength increases because of flux freezing. Magnetic pressure increases as B^2 , so eventually the magnetic pressure prevents the gas from condensing further. This limits the compression of gas behind the shock and over the latter stages of its evolution the magnetic field greatly increases the shell thickness relative to the idealized nonmagnetic case. Moreover, on the full scale of the shell the magnetic field acts as a retarding force, increasing the deceleration of the shell and reducing its final size (Tomisaka 1990, Ferrière et al. 1991, Slavin & Cox 1992). Also, the strong field can inhibit the production of worms (Heiles 1984) and chimneys (Norman & Ikeuchi 1989).

For the study and interpretation of magnetic fields, the size scale is paramount. At the largest scales within galaxies, the global scale, the issue is field generation and maintenance, and the underlying questions are “Primordial field or dynamo?” and “What kind of dynamo?”. These questions are addressed by size scales ranging down to spiral arms. At smaller sizes we have the field in individual interstellar diffuse structures, which are shaped by point energy injection and condensation onto molecular clouds. At yet smaller scales we have molecular clouds, especially those that contain protostellar cores. At the smallest scales we have regions where stars have formed.

This review concentrates on the magnetic field at intermediate and small size scales, i.e. diffuse H I structures and molecular clouds and cores. See Beck (2001) for discussion of magnetic fields on larger scales.

Our chosen size range is where energy input to the ISM occurs and where energy is transferred by turbulence to smaller scales and across cloud boundaries. There are three, and only three, established³ tracers for the field at these scales: polarization from aligned dust grains, which both absorb starlight and emit in the far-infrared, linear polarization of spectral lines, and Zeeman splitting of spectral lines. We will briefly include starlight polarization in Sect. 2.1, concentrate on Zeeman splitting of the 21-cm line in Sects. 4 and 5, and discuss magnetic fields in molecular clouds starting with Sect. 6.

One major focus of this review is the magnetic field in the diffuse H I. The H I resides in two thermal phases, the Cold Neutral Medium (CNM) and the Warm Neutral Medium (WNM), each containing roughly half of the total H I. Classically, we imagine these as points of stable isobaric thermodynamic equilibrium (Field 1965, McKee & Ostriker 1977), with the temperatures differing by about two orders of magnitude. The CNM does, in fact, reside in the classical stable thermal equilibrium. However, the WNM is buffeted by many agents on a range of timescales, so much so that at least 50% of the WNM has temperature smaller than 5000 K, meaning that it is *not* thermally stable (Heiles & Troland 2003). The WNM, being of much higher temperature and lower density, occupies the lion's share of the interstellar volume, roughly half the volume in the Solar vicinity (Heiles 2000b). H I Zeeman splitting measurements refer almost exclusively to the CNM: the line widths of the WNM are large, and when combined with H I angular structure the instrumental effects have so far prohibited reliable measurements.

The other major focus is the magnetic field in molecular clouds. The most important goal is to understand the role that magnetic fields play in the fundamental astrophysical process of star formation. One view is that self-gravitating clouds are supported against collapse by magnetic fields, with ambipolar diffusion reducing support in cores and hence driving star formation (Mouschovias & Ciolek 1999). The other view is that clouds form and disperse by the operation of compressible turbulence (e.g., Elmegreen 2000), with clumps sometimes becoming gravitationally bound and collapsing to form stars. The issue of which (if either) of these paradigms for the evolution of molecular clouds and the formation of stars is correct is currently unresolved. We describe the state of observations of magnetic fields in molecular clouds and how these data may be used to test predictions of the two star formation paradigms.

³ Use of the difference in line widths between neutral and ionized species to infer the angle between the line of sight and the magnetic field (Houde et al. 2002) and Faraday screens in dark-cloud envelopes (Wolleben & Reich 2004) are possible additional techniques that have not yet been fully accepted.

2 Measuring the Magnetic Field in Diffuse H I and Molecular Clouds

2.1 Polarization of Starlight by Magnetically Aligned Grains

Polarization of starlight holds the enviable position of being the means by which the interstellar magnetic field was discovered (see Davis & Greenstein (1951) for references and the original theory of grain alignment). Their alignment mechanism involves charged, spinning interstellar grains whose angular momentum vector component parallel to the field is damped by paramagnetic relaxation. The theory evolved with the introduction of superthermal spins and internal damping from Barnett relaxation (Purcell 1979, Purcell & Spitzer 1971). The theory continues to evolve as more exotic effects are uncovered (see Lazarian (2003) for a comprehensive review devoted exclusively to grain alignment; also see Draine (2003) and references quoted therein). In principle, the starlight polarization can be either parallel or perpendicular to B_{\perp} , the field on the plane of the sky. However, empirically the polarization is parallel to the field, as revealed by polarization in diffuse regions near the Galactic plane: B_{\perp} is parallel to the plane as expected for the Galactic-wide field.

Starlight polarization is produced by aligned dust that selectively absorbs one direction of linear polarization more than the orthogonal one. This makes the fractional polarization proportional to the extinction – we can't have polarization without extinction! Commonly, maps represent starlight polarization with lines whose direction is that of the polarization and whose length is proportional to the fractional polarization. The eye notices the long lines, which emphasize high extinction; these stars tend to be more distant. This is normally not the kind of bias one wants. For example, if we are interested in the nearby field structure, it is better to make all lines the same length. Accordingly, in our Fig. 1, we de-emphasize distant or high-extinction stars by placing an upper limit on the length of the lines.

The fractional starlight polarization also increases as the field becomes perpendicular to the line of sight. The dependence is $(B_{\perp}/B_{\text{tot}})^2$. From our discussion in Sect. 3.1, for randomly oriented fields this ratio has mean value 0.67 and median 0.87. With these high numbers, most of the regions have a high ratio, so in a statistical sample the fractional polarization is relatively weakly affected by the tilt of the magnetic field. Statistically, extinction is much more important in determining the fractional polarization.

Figure 1 shows the polarization of 8662 stars from the compilation of known catalogs (Heiles 2000a). The orientation of each star's polarization is indicated by a short line whose length L in great-circle degrees is $L = [4 < 2P]^{\circ}$, where P is the percentage polarization; we cap L at 4° to reduce the eye's preference for distant stars and, also, so that the lines don't become unrecognizably long. The assembly of lines is like iron filings near a bar magnet and traces out the plane-of-the-sky field lines. Note that these lines aren't

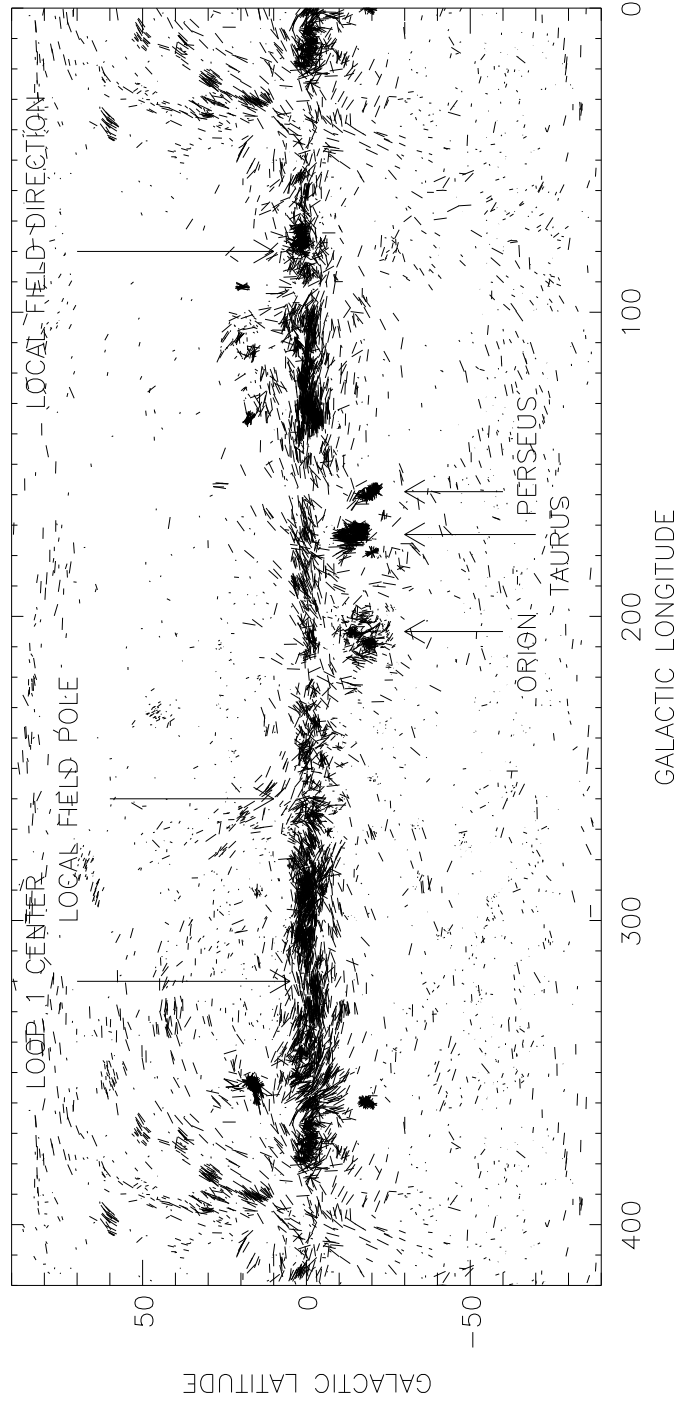


Fig. 1. Starlight polarization of 8662 stars. The orientation of each star’s polarization is indicated by a short line whose length L in great-circle degrees is $L = [4 < 2P]^\circ$, where P is the percentage polarization; for L , we plot whichever of the two quantities is smaller.

vectors, because they don't indicate direction; linear polarization is defined only modulo 180° , not 360° , so it only has an orientation.

Figure 1 shows the major large-scale features in the magnetic sky:

1. In the Galactic plane, the lines tend to be parallel to the plane, showing that the large-scale field lies in the plane. This is expected, if only from the effects of differential rotation and flux freezing.
2. Near $\ell = (80^\circ, 260^\circ)$ the lines lose this tendency. Heiles (1996a) used this observed effect to determine the direction and curvature of the local magnetic field: it points towards $\ell \sim 83^\circ \pm 4.1^\circ$ and has radius of curvature 8.8 ± 1.8 kpc.
3. Figure 1 shows several small areas where the density of measurements is so high as to obliterate the individual lines. These are regions of particular interest because of their dense clouds or star formation. We label Orion, Taurus, and Perseus, but several others also stand out. In these regions the dense clouds often look filamentary.

The observed stellar polarizations sometimes exhibit good alignment with filamentary structures, but the sense of alignment is not always the same. Three particularly good examples are Pereyra & Magalhaes (2004) and Fig. 5 in Heyer et al. (1987), where the polarizations are strikingly perpendicular to the long axis of the filaments, and Plate IX in Vrba et al. (1976), where the polarizations are parallel. The proper interpretation of these completely orthogonal senses of alignment *probably* consists of the following:

- a) Interstellar "filaments" are edge-on sheets.
 - b) Molecular clouds are flattened triaxial ellipsoids, which are often flattened enough to be considered as slabs (Sect. 8.2 below).
 - c) Fat interstellar filaments are the projections of flattened ellipsoids at random angles onto the plane of the sky.
 - d) The apparent orientation of B_\perp for such ellipsoids can adopt any position angle (call it Ψ) because of projection effects, as emphasized in the very important article by Basu (2000).
 - e) The only reliable way to determine the orientation of field lines with respect to the flattened ellipsoids is to compare the observed histogram Ψ for a large sample with model probability distributions for Ψ , such as Basu's. Not enough regions have been measured to accumulate sufficiently large-number statistics on Ψ . In particular, we caution that statements like "the observed B_\perp is perpendicular to the filament, i.e. perpendicular to the edge-on sheet" can be misleading when applied to a single example and can only have validity when applied to a good statistical sample.
4. Figure 1 shows the prominent distortion of the local field produced by Loop I (also known as the North Polar Spur). This distortion is also visible in the H I line and radio synchrotron continuum. It is the result of a superbubble produced by stellar winds and supernovae in the Sco/Cen

association; the overall morphology of the H I, hot gas (from its X-ray emission), and magnetic field (from radio synchrotron emission) strikingly confirms the concept that the ISM is shaped by such explosions. The center of Loop I appears in different places for the radio continuum (near $(\ell, b) \sim (329^\circ, 18^\circ)$ (Berkhuijsen et al. 1971) and for the H I (near $(320^\circ, 5^\circ)$ (Heiles 1998b). The causes for this difference are not currently understood.

Note our discussion of the field distortion by superbubbles in Sect. 5.4. The case here, with Loop I, is clear-cut because the ambient field lies predominantly across the line of sight. Other geometries are less clear and more complicated.

5. There are other large scale patterns in Fig. 1, which presumably trace other supernova shells or supershells. There is ample opportunity for further research here!

2.2 Polarization of Thermal Grain Emission

Starlight polarization occupies a high position, not only because of its historical importance but also because stars serve as distance markers. However, as with any tracer dependent on background sources, it is not very useful for mapping. Thermal radiation from dust is polarized, again because of the alignment of dust grains. We can look forward to the day when (1) enough stellar extinction measurements exist to determine the evolution of extinction with distance along arbitrary lines of sight, and (2) the mapping of IR emission from the diffuse interstellar gas starts in earnest. Unfortunately, (1) is in its infancy, except for particularly well defined clouds of high extinction, and regarding (2) no IR polarization data exist at all for diffuse regions.

In dense regions, however, far-infrared and millimeter wavelength observations of linearly polarized dust emission may be used to map the morphology of the magnetic field projected onto the plane of the sky, B_\perp (Hildebrand 1988). The position angle of maximum emission will be perpendicular to B_\perp . The mm-wavelengths sample the larger aligned grains and have the advantage that local star formation is not required because mm-wavelength emission occurs even with cold grains. These are particularly useful for places where stars have formed, because they heat the dust and provide strong emission. These regions are discussed later in this review. Other recent reviews which cover these aspects very well are Hildebrand et al. (2000), Hildebrand (2002), and Crutcher et al. (2003).

It is not possible to measure directly the strength of B_\perp since fairly weak magnetic fields can align grains, so the degree of polarization is not a measure of field strength. However, in the early days of interstellar polarization studies, Chandrasekhar and Fermi (1953) suggested that analysis of the small-scale randomness of magnetic field lines could yield estimates of the field strengths. The method depends on the fact that turbulent motions will lead to irregular magnetic fields (since under interstellar conditions fields will be frozen into the matter). There will therefore be a perturbed or MHD-wave component to the

field that should show up as an irregular scatter in polarization position angles relative to those that would be produced by a regular magnetic field. The stronger the regular field, the more it resists being irregularized by turbulence. They showed that the magnitude of the irregularity of field lines could yield the regular field strength in the plane of the sky:

$$B_{\perp} = Q\sqrt{4\pi\rho} \frac{\delta V}{\delta\phi} \approx 9.3\sqrt{n(H_2)} \frac{\Delta V}{\delta\phi} \mu G, \quad (1)$$

where $\rho = mn(H_2)$ is the gas density, δV is the velocity dispersion, $\delta\phi$ is the dispersion in polarization position angles in degrees, Q is a factor of order unity, $n(H_2)$ is the molecular hydrogen density in molecules cm^{-3} , and $\Delta V = \sqrt{8\ln 2} \delta V$ is the FWHM line width in km s^{-1} . Here we have used $Q = 0.5$, a calibration based on study of simulations of interstellar clouds by Ostriker, Stone, and Gammie (2001), but see also Heitsch et al. (2001) and Padoan et al. (2001). These simulations found that this method could yield reliable results in molecular clouds if $\delta\phi < 25^\circ$. One should note that while fluctuations in the field along the line of sight will be smoothed out by the polarization measurements, the calibration by the simulations referred to above include this in the Q factor. Heitsch et al. (2001) studied the effects of smoothing due to inadequate spatial resolution in the plane of the sky; although such smoothing will produce too large an estimate of B_{\perp} , the problem can be overcome so long as the region being studied, i.e. a molecular cloud or core, is adequately (a few resolution elements) resolved. The Chandrasekhar-Fermi method of estimating B is a statistical one that may be in error by ~ 2 for an individual cloud.

2.3 Spectral-line linear polarization

Linear polarization may also arise in radio-frequency spectral lines formed in the interstellar medium, even when Zeeman splitting is negligible. This Goldreich-Kylafis effect (Goldreich and Kylafis 1981, Kylafis 1983) may be used to probe magnetic field morphologies in molecular clouds. Heiles et al. (1993) provide a qualitative discussion of how the linear polarization arises. The direction of the polarization can be either parallel or perpendicular to the magnetic field, depending on the relationship between the line of sight, the direction of the magnetic field, and the direction of a velocity gradient that produces the anisotropic line optical depth that is required to produce linear polarization. Although the theory makes specific predictions for whether the field is parallel or perpendicular to the line polarization, in general the observations do not provide all of the necessary information. This ambiguity is unfortunate, but if structure in a cloud causes a flip by 90° in the polarization direction, it would easily be recognized and not confused with random magnetic fields. It therefore is a valuable tool in the measurement of magnetic field direction and in the degree of randomness of the field. As is the case for

dust polarization, the Chandrasekhar-Fermi method may be applied to maps of spectral-line linear polarization to estimate field strengths.

2.4 Zeeman Splitting

Interstellar magnetic fields are very weak and in all cases except masers produce Zeeman splitting $\Delta\nu_Z$ that is much smaller than the line width $\delta\nu$, so we usually have $\Delta\nu_Z/\delta\nu \ll 1$. This makes Zeeman splitting observations sensitivity limited. Accordingly, the only hope of detecting the splitting is with an atom or molecule whose splitting is “large”, i.e. \sim the Bohr magneton $e\hbar/2m_e c$; this, in turn, means that the molecule must have a large magnetic moment μ and Landé factor g . Thus, only species with electronic angular momentum are useful for Zeeman splitting observations. Other molecules have splitting \sim the nuclear magneton $e\hbar/2m_n c$, which is thousands of times smaller. There is one spectacular exception, water masers, where B_{\parallel} is tens of mG in regions having volume density $n \gtrsim 10^8 \text{ cm}^{-3}$ (Sarma et al. 2002).

For a given B_{\parallel} , the splitting $\Delta\nu_Z$ depends on g but is independent of the line frequency itself. For species with higher line frequencies, the line widths $\delta\nu$ rise proportionally, so for a given field strength the ratio $\Delta\nu_Z/\delta\nu$ decreases proportionally. This ratio is the crucial one for sensitivity, so in the absence of other considerations it is better to use low-frequency spectral lines. Heiles et al. (1993) describe the details and provide a list of atoms and molecules having electronic angular momentum. Suitable low-frequency ($< 11.2 \text{ GHz}$) species include H I, Radio Recombination Lines, OH, CH, C₄H, and C₂S. Other molecules have much higher frequencies, but experience shows that this is not always devastating because they can exist in very dense regions where field strengths are high enough to compensate; the defining example is CN (Crutcher et al. 1999), with line frequency $\sim 114 \text{ GHz}$ and B_{\parallel} of several hundred μG in the Orion Molecular Cloud 1, two cores in DR21OH, and probably M17SW.

Although the Stokes parameters V, Q, and U for the Zeeman components provide in principle full information about magnetic field strength and direction, in practice full information on \mathbf{B} cannot be obtained owing to the extreme weakness of Q and U. For the usual small-splitting case $\Delta\nu_Z/\delta\nu \ll 1$, Zeeman splitting is detectable in the Stokes V spectrum, which is the difference between the two circular polarizations. The V spectrum has the shape of the first derivative of the line profile (the Stokes I spectrum) with an amplitude $\propto B_{\parallel}/\delta\nu$, where B_{\parallel} is the line-of-sight component of the field.

Why B_{\parallel} instead of B_{tot} ? Or, in colloquial terms, how do the interstellar atoms “know” where the observer is by arranging the splitting to reveal only the particular field component that is oriented towards the observer? The answer involves the directionality associated with the circularly polarized line intensity. In contrast, when $\Delta\nu_Z/\delta\nu > 1$ the observed effect is the full splitting $\Delta\nu_Z$, which is $\propto B_{\text{tot}}$, not B_{\parallel} . Crutcher et al. (1993) treat this question in detail and provide formulas for the general case.

As examples of Zeeman splitting detections, Figs. 2 and 3 illustrate Zeeman splitting for three sources from the Arecibo Millennium survey (Heiles & Troland 2004) in order of decreasing signal/noise. The top panel of Figure 2 shows Cas A [data from Hat Creek (HCRO)], with more than 100 hours of integration, and the bottom one shows Tau A (from Arecibo), with ~ 7 hours. Figure 3 shows 3C138 (from Arecibo) with ~ 17 hours. See Sect. 4 for discussion. Fig. 10 shows a molecular Zeeman detection for the 3-mm CN lines toward DR 21 (OH), and Figs. 11 and 12 show a molecular Zeeman detection and B_{\parallel} map for the 18-cm line of OH toward S 106.

3 Observed vs. Intrinsic Probability Density Functions

We begin our focus on data and their interpretation with a rather technical discussion of the probability density function (pdf) of observed components of magnetic field and how they relate to the total field strength. This turns out to be surprisingly important, and because this discussion has not appeared prominently in past literature we devote considerable attention to it.

3.1 Conversion of the Intrinsic $\phi(B_{\text{tot}})$ to the Observed $\psi(B_{\parallel})$ and $\psi(B_{\perp})$

Given a field strength B_{tot} which can be randomly oriented to the line of sight, what is the probability of finding an observed field strength B_{\parallel} ? Alternatively, this is equivalent to the simple case in which all clouds have the same B_{tot} , which is randomly oriented with respect to the observer. The line-of-sight component B_{\parallel} is

$$B_{\parallel} = B_{\text{tot}} \cos \theta , \quad (2)$$

where θ is the angle between the field direction and the line of sight. θ can run from 0 to π , but it's simpler and no less general to consider the smaller interval θ from 0 to $\pi/2$. In this case, the pdf of θ is the familiar

$$\phi_{\theta}(\theta) = \sin \theta \quad (3)$$

and we wish to know the pdf of B_{\parallel} , which is given by (see Trumpler & Weaver (1953) for a discussion of these conversions)

$$\psi(B_{\parallel}) = \phi_{\theta}[\theta(B_{\parallel})] \left| \frac{d[\theta(B_{\parallel})]}{dB_{\parallel}} \right| , \quad (4)$$

which gives

$$\psi(B_{\parallel}) = \begin{cases} \frac{1}{B_{\text{tot}}} & \text{if } 0 \leq B_{\parallel} \leq B_{\text{tot}} \\ 0 & \text{otherwise} \end{cases} . \quad (5)$$

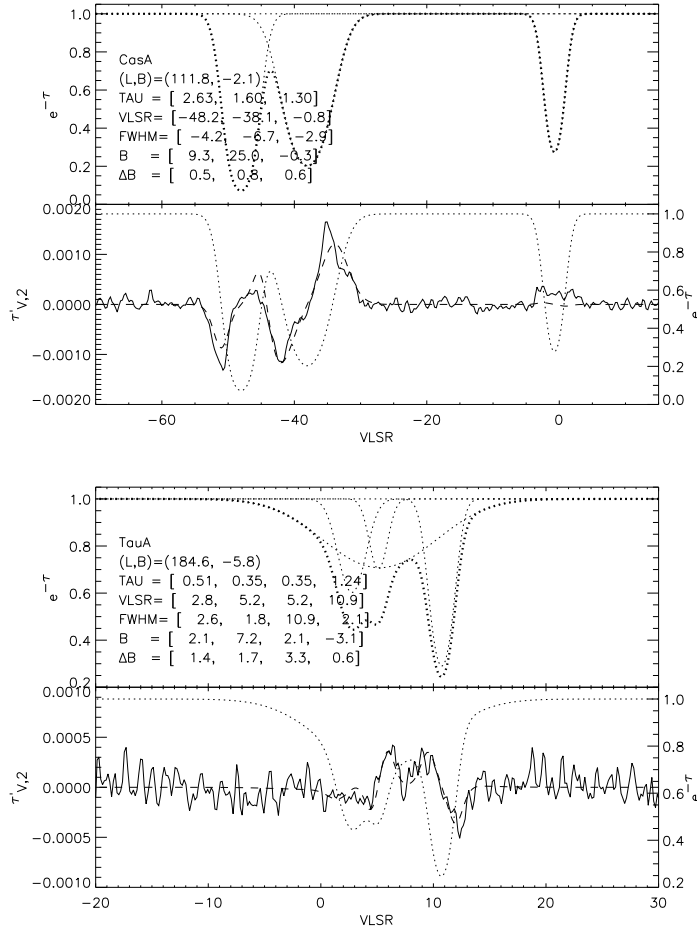


Fig. 2. Examples of H I Zeeman splitting for two sources in absorption from Heiles & Troland (2004). The **top panel** shows Cas A (data from HCRO). The **bottom panel** is Tau A. These are detections with very high signal/noise. See Sect. 4.2 for details.

In other words, B_{\parallel} is uniformly distributed between the maximum possible extremes 0 and B_{tot} (actually $\pm B_{\text{tot}}$). This leads to the well-known results that in a large statistical sample, both the median and the mean observed field strengths are half the total field strength and also $B_{\parallel}^2 = B_{\text{tot}}^2/3$. More generally, observed fields are always smaller than the actual total fields, and with significant probability they range all the way down to zero.

Similarly, we can derive the pdf for B_{\perp} , the plane-of-the-sky component; this is important for starlight polarization and synchrotron emissivity. We have

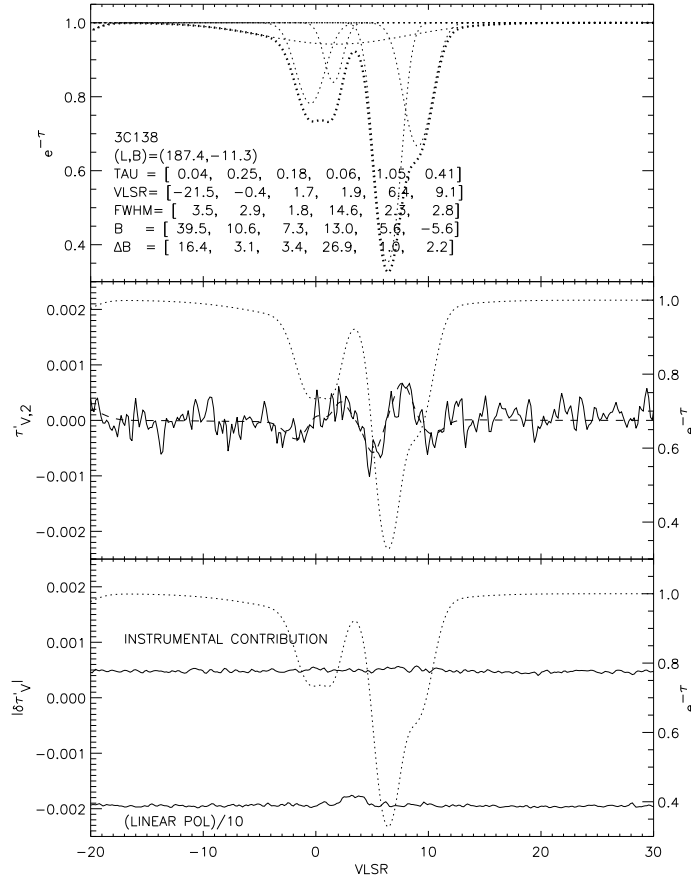


Fig. 3. An example of H I Zeeman splitting for 3C138 (Heiles & Troland 2004). This measurement has high signal/noise relative to most other results in the Millennium survey. See Sect. 4.2 for details.

$$\psi(B_{\perp}) = \begin{cases} \frac{B_{\perp}}{B_{\text{tot}}^2} \left[1 - \left(\frac{B_{\perp}}{B_{\text{tot}}} \right)^2 \right]^{-1/2} & \text{if } 0 \leq B_{\perp} \leq B_{\text{tot}} \\ 0 & \text{otherwise} \end{cases} . \quad (6)$$

The pdf $\psi \rightarrow \infty$ as $B_{\perp} \rightarrow B_{\text{tot}}$, but the cumulative distribution is well defined. The mean and median are $0.79 B_{\text{tot}}$ and $0.87 B_{\text{tot}}$, respectively; the high values reflect the large fraction of slabs tilted to the line of sight, where B_{\perp} is large. The mean of B_{\perp}^2 is $2/3 B_{\text{tot}}^2$.

The above applies if all B_{tot} are the same. Now suppose B_{tot} has an arbitrary pdf $\phi(B_{\text{tot}})$. Again, following standard techniques, we obtain

$$\psi(B_{\parallel}) = \int_{[B_{\parallel} > B_{\text{tot} \min}]}^{\infty} \frac{\phi(B_{\text{tot}})}{B_{\text{tot}}} dB_{\text{tot}} , \quad (7)$$

where the symbol $[B_{\parallel} > B_{\text{tot} \min}]$ means the larger of the two quantities. The presence of B_{tot} in the denominator means that smaller ranges of B_{\parallel} are emphasized. This is an obvious consequence of (5)'s uniform pdf for a single field value.

Similarly, for B_{\perp} we obtain the more complicated

$$\psi(B_{\perp}) = \int_{B_{\perp}}^{\infty} \frac{B_{\perp}}{B_{\text{tot}}^2} \left[1 - \left(\frac{B_{\perp}}{B_{\text{tot}}} \right)^2 \right]^{-1/2} \phi(B_{\text{tot}}) dB_{\text{tot}} . \quad (8)$$

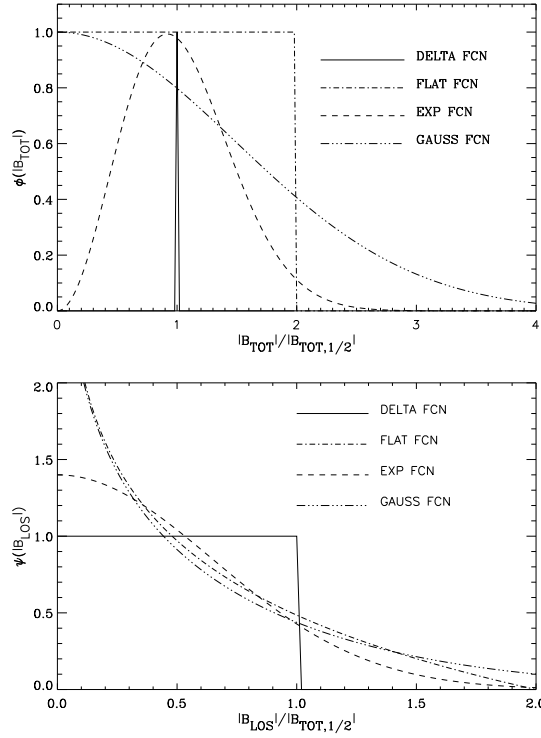


Fig. 4. Top panel: The intrinsic $\phi(B_{\text{tot}})$ for four representative functional forms. Bottom panel: their line-of-sight counterparts $\psi(B_{\text{los}})$. The vertical scales are arbitrary.

It's worth illustrating these equations with some examples. Figure 4 illustrates the solution of equation 7 for four functional forms of $\phi(B_{\text{tot}})$ plotted

against $\frac{|B|}{|B_{1/2}|}$, where the subscript 1/2 denotes the median value. These forms include the following:

1. $\phi(B_{\text{tot}})$ a Kronecker delta function (DELTA FCN), $\phi(B_{\text{tot}}) = \delta(B_{\text{tot}} - B_{\text{tot},0})$, yielding ψ a flat function (as discussed immediately above, equation 5);
2. $\phi(B_{\text{tot}})$ a flat distribution (FLAT FCN) between $0 \leq |B_{\text{tot}}| \leq B_0$, yielding $\psi \propto \ln\left(\frac{B_0}{B_{\text{los}}}\right)$;
3. $\phi(B_{\text{tot}})$ a weighted Gaussian (EXP FCN),

$$\phi(B_{\text{tot}}) = \sqrt{\frac{2}{\pi B_0^2}} \frac{B_{\text{tot}}^2}{2B_0^2} e^{-(B_{\text{tot}}^2/2B_0^2)}, \quad (9)$$

yielding ψ a Gaussian with dispersion B_0 .

4. $\phi(B_{\text{tot}})$ a Gaussian (GAUSS FCN) with dispersion B_0 , yielding $\psi \propto E_1\left(\frac{B_{\text{los}}^2}{2B_0^2}\right)$, where E_1 is the exponential integral of order 1.

All four $\phi(B_{\text{tot}})$ are plotted with respect to $\frac{B_{\text{tot}}}{B_{\text{tot},1/2}}$, so the medians of all lie at unity on the x -axis. However, the means differ. Similarly, the medians and means of the associated $\psi(B_{\text{los}})$ differ from each other. These relationships between median and mean are summarized in Table 1. The medians and means for $\psi(B_{\text{los}})$ are all about half those for $\phi(B_{\text{tot}})$, which is a direct result of the weighting by B_{tot}^{-1} in equation 7.

Table 1. MEDIAN AND MEAN VALUES FOR REPRESENTATIVE PDFS

$\phi(B_{\text{tot}})$	$B_{\text{tot},1/2}$	$\langle B_{\text{tot}} \rangle$	$B_{\text{los},1/2}$	$\langle B_{\text{los}} \rangle$
DELTA FCN	1.00	1.00	0.50	0.50
FLAT FCN	1.00	1.00	0.40	0.52
GAUSS FCN	1.00	1.18	0.38	0.59
EXP FCN	1.00	1.04	0.44	0.51

Figure 4 is disappointing from the observer’s standpoint, because the observed distributions $\psi(B_{\text{los}})$ do not differ very much. These differences become smaller—inconsequential, in fact—when there is some measurement noise. Unfortunately, given the inevitable errors in *any* observation that is sensitive to B_{los} , it seems practically impossible to distinguish among different functional forms for $\phi(B_{\text{tot}})$. Nevertheless, the average value of B_{los} is close to half the average value of B_{tot} for a wide range of intrinsic pdfs of the latter; this also applies to the medians, but less accurately. Therefore, this rule of thumb may be used to estimate the median or average B_{tot} from an ensemble of measurements of B_{los} .

3.2 Conversion of the Intrinsic $\phi[\log(B_{\text{tot}})]$ to $\psi[\log(B_{\parallel})]$

Sometimes people treat $\log(B_{\parallel})$, instead of B_{\parallel} , as the important quantity. In particular, in Sect. 8.2 below, we consider least square fits of $\log(B_{\parallel})$ for molecular clouds. The statistics for $\log(B_{\parallel})$ differ from those of B_{\parallel} . Carrying through the usual analysis, we find for the analog to (5)

$$\psi \left[\log \left(\frac{B_{\parallel}}{B_{\text{tot}}} \right) \right] = \ln(10) 10^{\log \left(\frac{B_{\parallel}}{B_{\text{tot}}} \right)} . \quad (10)$$

The mean and median of $[\log(B_{\parallel}/B_{\text{tot}})]$ are -0.434 and -0.693 , which correspond to $B_{\parallel}/B_{\text{tot}} = 0.37$ and 0.21 , respectively. Thus the statistics of $\log B_{\text{tot}}$ favor smaller means and medians than do those of B_{tot} , for which both numbers are 0.5 .

3.3 Conversion of the Intrinsic $\phi(N_{\perp})$ to the Observed $\psi(N_{\text{obs}})$ for Sheets

Many interstellar morphological structures are sheets. Examples for H I include two sheets mapped in 21-cm line emission (Heiles 1967), and an extreme sheet with aspect ratio of several hundred (Heiles & Troland 2003). Along with Heiles & Troland (2003), we consider that all CNM structures are best considered as sheets.

As we did with the field, we discuss the pdfs of the observed column density for sheets (N_{obs}) given the total H I column density N_{\perp} in the direction perpendicular to the sheet, again assuming random orientations. If the normal vector to the sheet is oriented at angle θ with respect to the line of sight, then we have

$$N_{\text{obs}} = \frac{N_{\perp}}{\cos \theta} . \quad (11)$$

If all sheets have the same N_{\perp} , then

$$\psi(N_{\text{obs}}) = \begin{cases} \frac{N_{\perp}}{N_{\text{obs}}^2} & \text{if } N_{\text{obs}} \geq N_{\perp} \\ 0 & \text{otherwise} \end{cases} . \quad (12)$$

For a single N_{\perp} , N_{obs} has a long tail extending to infinity. The mean value of N_{obs} is not defined because, with infinite sheets, the integral diverges logarithmically; of course, this doesn't occur in the real world, where sheets don't extend to infinity. The median value of N_{obs} is $2N_{\perp}$, reflecting the increased observed column for tilted sheets. For an arbitrary pdf $\phi(N_{\perp})$ we obtain

$$\psi(N_{\text{obs}}) = \frac{1}{N_{\text{obs}}^2} \int_0^{[N_{\text{obs}} < N_{\perp \text{max}}]} N_{\perp} \phi(N_{\perp}) dN_{\perp} . \quad (13)$$

3.4 Conversion of the Intrinsic Bivariate Distribution $\phi(B_{\text{tot}}, N_{\perp})$ to the Observed $\psi(B_{\parallel}, N_{\text{obs}})$ for Sheets

We can reasonably expect the magnetic field to lie either parallel or perpendicular to the sheet. If the sheet has formed by coalescence of more diffuse gas flowing more easily along the field lines, then the field should lie perpendicular to the sheet. In contrast, if the sheet is the result of a shock that has swept up both the gas and magnetic field lines, then the field should lie parallel to the sheet. Accordingly, we are led to consider the bivariate distribution of magnetic field and column density for these two cases. We assume that B_{tot} , N_{\perp} , and of course θ are all uncorrelated. We again consider the illustrative case of delta functions for B_{tot} and N_{\perp} .

If B_{tot} is perpendicular to the sheet (the *perpendicular model*), then both B_{\parallel} and N_{\perp} depend only on $\cos\theta$, so the bivariate pdf degenerates to the deterministic line

$$B_{\parallel} = B_{\text{tot}} \frac{N_{\perp}}{N_{\text{obs}}} \quad (14)$$

which is shown in the top panel of Fig. 5. The parallel model, with B_{tot} lying in the sheet, is more complicated, with

$$\psi(B_{\parallel}, N_{\text{obs}}) = \frac{N_{\perp}}{\pi N_{\text{obs}}} [(B_{\text{tot}} N_{\text{obs}})^2 - (B_{\text{tot}} N_{\perp})^2 - (B_{\parallel} N_{\text{obs}})^2]^{-1/2}. \quad (15)$$

This is illustrated by the contours in the bottom panel of Fig. 5.

Discussion of Figure 5

The two panels of Fig. 5 exhibit the joint pdfs for the two sheet models (B_{tot} perpendicular and parallel to the sheets). The median observed column density $N_{\text{obs}1/2}$ is twice the assumed N_{\perp} and the median observed magnetic $B_{\parallel 1/2}$ is half the assumed B_{tot} ; these univariate medians are indicated by squares on the top two panels. The significance of these squares is that half the observed B_{\parallel} , and half the observed N_{obs} , are smaller and half larger. Finally, the dashed line in the middle panel exhibits the median $B_{\parallel 1/2}$ versus N_{obs} ; we calculate this by extracting the conditional pdf $\psi(B_{\parallel}|N_{\text{obs}})$ versus N_{obs} , and calculating the medians from its cumulative distributions.

The top and middle panels illustrate a crucial observational signature at large N_{obs} that distinguishes between the two sheet models: for the perpendicular model, large N_{obs} goes with small B_{\parallel} , and vice-versa for the parallel model. More quantitatively, for the perpendicular model, *all* of the datapoints having N_{obs} above its univariate median ($N_{\text{obs}} > N_{\text{obs}1/2}$, indicated by the square) have $B_{\parallel} < B_{\parallel 1/2}$. In contrast, for the parallel model *most* (66%) of the datapoints with $N_{\text{obs}} > N_{\text{obs}1/2}$ have $B_{\parallel} > B_{\parallel 1/2}$.

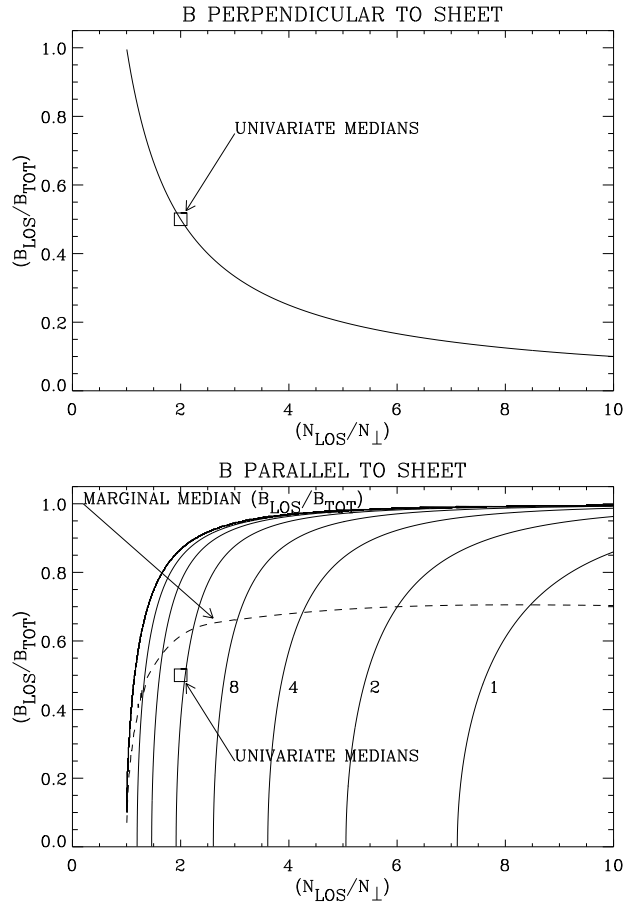


Fig. 5. The theoretical observed joint pdfs $\psi(B_{\parallel}, N_{\text{obs}})$ for the illustrative case of δ -function distributions for B_{\parallel} and N_{obs} . The **top panel** shows the pdf for B_{tot} perpendicular to the sheets; it degenerates into a single line. The **bottom panel** is for B_{tot} parallel to the sheets; contours are spaced by factors of 2 with arbitrary scaling, and the dashed line shows the median B_{\parallel} versus N_{obs} .

More precisely for the parallel model, as N_{obs} gets large, the marginal pdf $\psi(B_{\parallel} | N_{\text{obs}}) \rightarrow N_{\perp 0} / \pi N_{\text{obs}}^2 (B_{\text{tot}0}^2 - B_{\parallel}^2)^{-1/2}$, which produces the median $B_{\parallel 1/2} \rightarrow 0.71 B_{\text{tot}}$; this is the asymptote of the dashed line on the middle panel of Fig. 5.

3.5 Commentary

This discussion has been rather technical, more so than is usual in a review. However, the payoff follows because we can make some powerful inferences from this discussion.

1. Consider the one-dimensional $\psi(B_{\perp})$ for a given B_{tot} . $\psi(B_{\perp})$ diverges as $B_{\perp} \rightarrow B_{\text{tot}}$; the median and mean values of B_{\perp} are $0.79 B_{\text{tot}}$ and $0.87 B_{\text{tot}}$, respectively. Thus, maps of starlight polarization, or IR polarization of dust emission, tend to represent the full field strength to a considerable degree, a much higher degree than does Zeeman splitting for B_{\parallel} (see next paragraph).
2. Consider the one-dimensional $\psi(B_{\parallel})$ for a given B_{tot} . $\psi(B_{\parallel})$ is flat for $0 < B_{\parallel} < B_{\text{tot}}$. Suppose we have a collection of measured B_{\parallel} and can reasonably expect the orientation to be random. Suppose we wish to fit a dependence of magnetic field on, say, volume density, as we will do below in Sect. 8.2. Then we should *not* use the standard least squares technique because it assumes that the residuals from the mean have a Gaussian distribution; in contrast, the intrinsic distribution of residuals of B_{\parallel} is flat. In particular, this means that errors derived from the distribution of residuals to the fitted points are not calculated correctly.

Similarly, when fitting $\log B_{\parallel}$ the distribution of residuals is asymmetric, which introduces a systematic bias into the least-squares fitted result. This must be corrected for, as we do in Sect. 8.2 below. In addition, of course, the errors are also not calculated correctly.

3. Consider an assembly of B_{\parallel} from different sources, all of which have the same B_{tot} . Then we expect some B_{\parallel} to be very small. Thus, small values of B_{\parallel} do not necessarily mean that B_{tot} is small. Rather, an unbiased survey produces many small, undetectable values of B_{\parallel} , which can be very frustrating for the observer but is nevertheless inevitable. A spectacular example is the local-arm (0 km s^{-1}) field seen against Cas A (top panel Fig. 2), $B_{\parallel} = -0.3 \pm 0.6 \mu\text{G}$. This surprisingly small result is perfectly consistent with statistical expectation. Of course, we cannot rule out that the field actually is really small in any particular case like this, but one needs additional data to draw such a conclusion!
4. Consider the large set of magnetic fields observed in 21-cm line *emission* in morphologically obvious structures, reviewed below in Sect. 5.4. The term “morphologically obvious” means filaments or edge-on sheets. Edge-on sheets should be edge-on shocks in which the field is parallel to the sheet, i.e. with large θ . Here, the statistics reverse and favor relatively large B_{\parallel} . As explained in Sect. 3.4, as the line of sight becomes parallel to the sheet – i.e. for a morphologically obvious sheet – the median $B_{\text{tot}1/2} \rightarrow 0.71 B_{\text{tot}}$. For these structures, measured fields are strong, ranging from ~ 5 to $\sim 10 \mu\text{G}$. This is not inconsistent with a uniform $B_{\text{tot}} \sim 10 \mu\text{G}$, which is a factor of two above the median CNM field strength from Sect. 4. This suggests that shocks enhance the field strength, but not by large factors.

4 B_{\parallel} from H I Absorption Lines

Zeeman splitting of the H I line in absorption holds the enviable position of being the means by which the interstellar magnetic field *strength* was first measured (Verschuur 1969). With quantitative knowledge of the magnetic field strengths came the beginning of the end of the famous theorists’ refuge (“...the larger one’s ignorance, the stronger the magnetic field” (Woltjer 1967)).

Zeeman splitting in absorption, instead of emission, is enviable for another important reason. It is easier to measure B_{\parallel} in the CNM than in the WNM because the H I line opacity $\propto T^{-1}$, which makes the CNM appear prominently in absorption. We detect absorption by performing (*ON – OFF*) measurements against a radio continuum source; for such measurements the sidelobe contributions from the emission tend to cancel. This makes the CNM absorption results very much less subject to instrumental effects than emission results (Heiles & Troland 2004). In fact, we consider the results to be statistically reliable, with Gaussian-distributed uncertainties and small systematic errors.

4.1 Early Work

Verschuur’s (1969) discovery of Zeeman splitting in interstellar H I, in absorption against Cas A and Tau A, broke an earlier series of frustrating efforts focused at Jodrell Bank⁴. He continued making such measurements, but obtained physically interesting upper limits or measurements for only five sources, which he reviewed in 1974 (Verschuur 1974). Four of these sources had detections.

Most of Verschuur’s absorption detections do not refer to diffuse H I, but rather to molecular clouds or star-forming regions. Two of the four sources (Orion A and M17; $B_{\parallel} \sim -60$ and $+25 \mu\text{G}$ respectively) are dynamically active H II regions. One (two components in the Cas A Perseus arm with $B_{\parallel} \sim (+9, +25) \mu\text{G}$; Fig. 2) is a molecular cloud probably undergoing star formation (Troland et al. 1985, Schwarz et al. 1986). None of these refer to interstellar diffuse H I. For sources that sample the diffuse H I, we are left with a single detection: Tau A, with two velocity components having $B_{\parallel} \sim (-3, +7) \mu\text{G}$ (Fig. 2, Heiles & Troland 2004). Two other diffuse-cloud sources have only upper limits: Cygnus A, with $B_{\parallel} \lesssim 3.5 \mu\text{G}$, and Cas A Orion arm, with $B_{\parallel} \lesssim 1 \mu\text{G}$ (Fig. 2, Heiles & Troland 2004).

Contrary to the usual development of observational astronomy, Verschuur’s discovery was not followed by the establishment of a “cottage industry” that produced a large number of detections resulting in a significant expansion of

⁴ Verschuur made a typographical error in labeling the sign of his Stokes V profiles (but not his derived B_{\parallel}). In addition, higher sensitivity results (Fig. 2; also Heiles & Troland 2004) reveal more Gaussian components with detected fields.

HI absorption Zeeman splitting measurements. The reason is simply the weakness of the Zeeman splitting: typically $\Delta\nu_Z/\delta\nu \lesssim 10^{-3}$. This state of affairs lasted until the turn of the millennium (Heiles & Troland 2004).

4.2 Recent Work: the Arecibo Millennium Survey

In our recent Arecibo Millennium survey, we (Heiles & Troland 2004) have only 22 detections that exceed 2.5σ , out of a total of 69 measurements whose uncertainties are low enough to make them interesting. This weakness forces us to discuss the CNM Zeeman splitting results statistically. And fortunately, the statistical reliability allows us to actually carry through this statistical discussion.

Figures 2 and 3 exhibit three sources from the Millennium survey as examples of strong detections. The top two panels show Verschuur's original discovery sources Cas A and Tau A, but with higher sensitivity than his original spectra. The separate detections in two velocity components of the Perseus Arm, near -40 km s^{-1} , are very clear; the absence of a detection for the Orion arm near 0 km s^{-1} is also clear. For Taurus, there are multiple Gaussian components, more than one of which has associated features in Stokes V . The multiple-component aspect is also clear for 3C138. For these sources with multiple velocity components, we fit fields independently to each component (Heiles & Troland 2004). The dashed lines in the three Stokes V spectra show the fits.

We emphasize that these three sources have the strongest signal/noise in Stokes V in the entire sample. Mostly we obtain upper limits instead of detections for $B_{||}$. When we include only those for which the uncertainty $\Delta B_{||} < 10 \mu\text{G}$, the observed histogram $\psi(B_{||})$ resembles a Gaussian. Relating this to the intrinsic field B_{tot} is a complicated business requiring a Monte Carlo analysis. The end result is that the median B_{tot} is

$$B_{\text{tot},1/2} = 6.0 \pm 1.8 \mu\text{G} . \quad (16)$$

Not surprisingly from our earlier discussion, nothing can be said about the pdf $\phi(B_{\text{tot}})$.

4.3 Equipartition Between Magnetism and Turbulence in the CNM

There are no obvious correlations of $B_{||}$ with any quantity, including N_{obs} , linewidth, or T_k . However, we can compare energy densities.

Each CNM component in Heiles & Troland (2004) is characterized by measured values of not only magnetic field but also temperature, column density, and velocity dispersion. This allows us to compare energy densities. One way to do this is with the classical plasma parameter β , equal to the ratio of thermal to magnetic pressure or, alternatively, thermal to magnetic

energy density. We can similarly define the ratio of turbulent to magnetic energy density (Heiles & Troland 2004).

For comparison of turbulent and magnetic effects in the CNM, we calculate the relevant ratios for the following adopted parameter values, which are close to the medians:

$$T = 50 \text{ K} \quad (17)$$

$$\Delta V_{\text{turb,1d}} = 1.2 \text{ km s}^{-1} \quad (18)$$

$$B_{\text{tot}} = 6.0 \mu\text{G} \quad (19)$$

These values provide

$$\beta_{\text{th}} = 0.29 \quad (20)$$

and

$$\beta_{\text{turb}} = \frac{E_{\text{turb}}}{E_{\text{mag}}} = M_{\text{ALF,turb}}^2 = 1.3 . \quad (21)$$

These values should be regarded as representative. Not all CNM clouds have the median values, so these parameters have a considerable spread.

4.4 Field Strengths in the CNM Versus Those in Other Phases

As mentioned in Sect. 1, Beck (2001) reviews the most recent estimate of field strength derived from synchrotron emission, minimum energy arguments, Faraday rotation, and polarization. He finds the regular component to be $\sim 4 \mu\text{G}$ and the total component to be $\sim 6 \mu\text{G}$. The difference between regular and total components is the fluctuating component, whose scale length is probably at least tens of parsecs. Because our CNM structures are physically small, it is more appropriate to compare their field strengths with the total component. The CNM median of $\sim 6 \mu\text{G}$ is nominally identical to Beck's local Galactic total component of $\sim 6 \mu\text{G}$.

All of the other diffuse ISM phases are less dense than the CNM. For example, both the WNM and the WIM are nearly two orders of magnitude less dense. Thus the ISM field strength does not depend very sensitively on volume density. In contrast, for the larger densities associated with molecular clouds, in which gravity plays a significant role, the field strength does increase with density, roughly $B_{\text{tot}} \propto n^{1/2}$ (Crutcher 1999). The density independence for diffuse gas is well known from past studies (Crutcher et al. 2003), so this is hardly news; nevertheless, we tend to forget these things and, moreover, from an observer's standpoint the paucity of detectable fields is disappointing.

4.5 Astrophilosophical Discussion

These numbers indicate that magnetism and turbulence are in approximate equipartition. The approximate equipartition suggests that turbulence and magnetism are intimately related by mutual exchange of energy. Magnetic energies do not dissipate because the magnetic field cannot decay on short time scales. On the contrary, supersonic turbulence does dissipate rapidly: numerical simulations of turbulence suggest that the magnetic field does not mitigate turbulent dissipation (MacLow et al. 1998). Thus, the equipartition between the dissipative turbulent energy and nondissipative magnetic energy must arise from a mechanism other than energy decay.

We suspect the answer is that the CNM components result from the transient nature of turbulent flow: the CNM occupies regions where densities are high, produced by converging flows, and the density rise is limited by pressure forces. This idea is discussed and reviewed thoroughly by MacLow & Klessen (2004). These limiting pressures are magnetic because the gas has small β_{th} , meaning that thermal pressure is negligible and the dynamical equality makes the magnetic pressure comparable to the converging ram pressure. The equipartition looks like a steady-state equilibrium, but it is really a snapshot of time-varying density fields and our immediate observational view is a statistical result over a large sample. In other words, our current observational snapshot shows an ensemble at a given time. Against this we compare the numerical simulations, which are stationary in the sense that they have been allowed to run long enough that the statistical properties become time-independent. Such simulations are also ergodic, with statistical properties over time being equivalent to those over space. With this view, the ISM dynamically evolves through turbulence and its properties are governed by statistical equilibrium of energy inputs and dissipation.

An alternative picture is based on the classical model of *static equilibrium* in which all forces balance. Static clouds are formed and evolve by gas moving adiabatically from one equilibrium state to another as ambipolar diffusion allows magnetic flux to slowly unfreeze. These slow adjustments in morphology occur primarily along the field lines. At each stage there is a well-defined morphological structure in quasistatic equilibrium. This idea was originated by Mouschovias (1976) and has been well-developed by the “Mouschovias school” of students and collaborators, consisting of Ciolek, Fiedler, and Basu (see Ciolek & Basu 2000 and references quoted therein), and by Shu and collaborators (see Shu et al. 1999). The picture of static equilibrium predicts the linear relationship between B_{tot} and $\sigma_v n^{1/2}$, which is found for molecular clouds (Sect. 8.2 below), which is equivalent to the energy equipartition found in (21) above.

Both models predict the same result, namely approximate equipartition between turbulent and magnetic energy densities. However, the concepts on which they are based are in direct opposition. Which one is correct for diffuse clouds? The role of gravity in diffuse clouds is negligible. Given this, the

static equilibrium models, for which gravity is a major player, cannot apply to diffuse clouds. Thus, for diffuse gas (but not for molecular clouds) we favor the concept of statistical equilibrium as briefly outlined above. Analytical and numerical research is being intently pursued on this topic; an excellent review is MacLow & Klessen (2004).

5 $B_{||}$ from H I Emission Lines

Zeeman splitting of the H I line in emission holds the enviable position of not requiring a background source: one can look anywhere, so that the field in interesting regions can be measured and mapped. However, nothing comes for free: emission measurements are prone to instrumental error from polarized sidelobes. These errors have been the subject of much controversy and here we will devote considerable attention to explaining these matters. We will conclude that most published Zeeman detections in H I emission are fairly reliable. We begin our examination of this question with a discussion of instrumental effects arising from polarized structure in the telescope beam.

5.1 Instrumental Effects from Polarized Sidelobes and their Description by a Taylor Series

The instrumental effects in H I Zeeman splitting measurements arise from angular structure in the Stokes V beam interacting with H I structure on the sky. The V beam has angular structure, even to the extent of having sign changes. Troland & Heiles (1982) used both their empirical investigations of the HCRO telescope and theoretical investigations published by others to classify this V structure into three primary categories; here we split one, the sidelobe component, into two subcomponents, near and far sidelobes. This gives:

1. *Beam squint*, in which the two circular polarizations point in slightly different directions with typical separation (Ψ_{BS}) of a few arcseconds. This angular separation doesn't seem like much, but given a small velocity gradient with position the two beams see different frequencies, and this mimics the tiny splitting resulting from the Zeeman effect.
2. *Beam squash*, in which the Stokes V beam has slightly different beamwidths in orthogonal directions. These "four-lobed" polarized beams, in which two lobes on opposite sides of beam center have the same sign and two lobes rotated 90° in position angle have the opposite sign, are sometimes described as "cloverleaves". This four-lobed structure responds to the second derivative of the 21-cm line on the sky. Theoretically, beam squash occurs only for the linearly polarized Stokes parameters Q and U , but in practice it can also for Stokes V (e.g. Heiles et al. 2001, Heiles et al. 2003).

3. *Near-in sidelobes*, which can be considered as standard diffraction effects and have polarization structure similar to that of the main beam described above.
4. *Far-out sidelobes*. For most telescopes the total power in these “distant sidelobes” is nontrivial: even though the sidelobes are weak, they cover very large solid angles and tend to be elliptically polarized. Troland and Heiles (1982) present one of the very few, perhaps the only, map of the circular polarization of far-out sidelobes; the pattern looks like a windmill and obviously results from feed legs. These distant sidelobes are a result of telescope surface roughness and the feed leg structure, so their structure is impossible to predict and can be time variable.

The classification is useful because it allows one to parameterize the beam polarization effects. These parameters can be measured and corrections applied. Nearly all H I emission Zeeman splitting measurements have made these corrections in one form or another.

The appropriateness of this fourfold classification applies to all telescopes that have been used for emission Zeeman splitting observations: HCRO (Heiles 1996b), the Green Bank 140-foot telescope (Verschuur 1969, 1989), Arecibo (Heiles et al. 2001), and the Green Bank Telescope (GBT) (Heiles et al. 2003). For example, Verschuur’s (1969) Fig. 2 presents the V beam pattern for the 140-foot telescope as it was in the late 1960’s. At that time, it was very well described by beam squint with a peak-to-peak amplitude of about 1.4%; this corresponds to a beam squint $\Psi_{BS} \approx 7''$. Our maps of the complete polarized sidelobe structure of the HCRO telescope always produced similar results, although with much smaller beam squint. Verschuur’s (1989) Fig. 1 presents the 140-foot polarized beam structure as it was in the late 1980’s, and shows a drastic difference: the newer map shows primarily the four-lobed pattern of our category (2) with little beam squint. (The feed system had been changed between the two epochs.) The 1960’s version of the beam pattern made the 140-foot telescope unsuitable for Zeeman-splitting measurements of H I in emission because the beam squint contribution to instrumental error would have been excessive. However, the 1980’s version, with its small beam squint but higher second-derivative component, was satisfactory – as shown by the fact that Verschuur reobserved four positions that had previously been observed with the HCRO telescope and found excellent agreement in three.

5.2 Verschuur’s Bombshell

Measurements of Zeeman splitting of H I emission lines have been made by Troland, Heiles and other collaborators, and Verschuur. Until 1993, the agreement was quite good.

Despite the apparent agreement of the measurements, in 1993 Verschuur became highly suspicious of all emission results and dropped a bombshell. He asserted that “. . . claims of Zeeman effect detections in H I emission features

... based on observations made with presently available single-dish radio telescopes cannot be regarded as reliable.” At the time of his paper, the HCRO telescope had already been destroyed, but he meant his claim to apply to that telescope as well as other telescopes that were then available. This is a strong statement and it has had a dampening effect on the field, making many astronomers highly suspicious of the published results. Accordingly, we believe a thorough discussion is in order. This discussion is excerpted from Heiles (1998a), a reference which is difficult to find.

We believe Verschuur’s claim to be incorrect. His claim is based on his estimates of the instrumental effects, which in turn are based *solely* on measurements of the velocity gradient of the H I line (Verschuur 1995a,b). In particular, his estimates of the instrumental effects are not based at all on the *properties of the polarized beam*. To clarify his procedure and its inadequacy, we describe its six steps:

1. Observe V and I spectra at the central position P; denote these $V_{\text{obs}}(v)$ and $I_{\text{obs}}(v)$.
2. Make an 8-point map of I spectra around P. Each map position is displaced from P by $15'$; in position angle the 8 points are equally spaced (45°), with the displacements of 4 points towards the cardinal directions in equatorial coordinates.
3. Find the pair of profiles whose difference spectrum $\Delta(v)$ is strongest and mimics the shape of $V_{\text{obs}}(v)$.
4. Find the coefficient R that scales the $\Delta(v)$ spectrum to the V_{obs} spectrum, i.e. the best fit for $R\Delta(v) = V_{\text{obs}}(v)$.
5. Produce the “corrected” V spectrum $V_{\text{corr}}(v) = V_{\text{obs}}(v) - R\Delta(v)$.
6. Derive the Zeeman splitting from $V_{\text{corr}}(v)$.

The fatal flaw is that R , which represents the beam squint, is not measured directly for the *telescope*. Rather, it is given the particular value that minimizes the observed V spectrum $V_{\text{obs}}(v)$.

As explained above, the beam squint samples the first derivative of the 21-cm line on the sky, which must contain a velocity gradient at some level. Steps 2 and 3 of the above procedure measure the velocity gradient. Step 4 fits this velocity gradient to the observed V spectrum and derives the coefficient R . Then, no matter how large R is, it is used to subtract away the scaled Δ profile from the observed V spectrum. With this step, R implicitly represents the amplitude of the beam squint in units of $30'$.

But the amplitude of the beam squint can be independently measured for a telescope. The proper procedure would be to measure the beam squint and velocity gradient, multiply the two vectorially, and subtract the result from the observed V spectrum.

Consider one particular entry in Verschuur’s (1995b) Table 2 as an example: NCPShell.4. For this position he obtains $R = 0.0052$. This corresponds to a beam squint of $(30' \times 0.0052) = 9'.4$. He uses this value of R to subtract away a velocity derivative from the V_{obs} profile that amounts to $10.8 \mu\text{G}$, obtaining

a “corrected” field strength $2.1 \pm 1.0 \mu\text{G}$. In doing this he has removed the contribution to V_{obs} that arises from the magnetic field – he has removed the “signal”. In colloquial English, this is known as “throwing out the baby with the bathwater”.

The data in Verschuur’s papers (1995a,b) could be reanalyzed taking account of the fact that the beam squint of the 140-foot telescope is limited to some maximum value. Unfortunately, this is not discussed by Verschuur, but judging from his earlier paper in this field (Verschuur 1989) the upper limit on 140-foot beam squint is probably $\sim 3''$, which corresponds to $R = 0.0017$ (0.17%). Many entries in Verschuur’s table have $R > 0.0017$ and these probably represent real measurements of Zeeman splitting.

5.3 Reliability of the HCRO H I Emission Results

Nearly all published results in H I emission are from the HCRO telescope. Verschuur’s bombshell was directed primarily at those results. Having dealt with Verschuur’s criticisms, it remains to show that our HCRO emission measurements are, in fact, correct. Heiles (1996b) discussed his correction procedures for the HCRO data. He also tested these correction procedures on the North Celestial Pole, which is the one point on the sky where, for the HCRO equatorially mounted telescope, the telescope beam could rotate in a complete circle.

Heiles divides the data into 12 time (“Right Ascension” or RA) bins and measures the magnetic field strength B_{\parallel} separately and independently for each. He then Fourier analyzes the 12 results. The Fourier terms respond differently to the beam components listed above. Beam squint, with a two-lobed pattern on the sky, works with the first derivative of the H I emission to produce one cycle of variation per 24 hours. Beam squash produces two cycles per 24 hours, and higher order terms can come from the sidelobes.

These Fourier coefficients constitute *empirically determined* squint and squash contributions for the NCP. He also *predicted* the squint contribution by measuring the first derivatives of the H I emission and applying the previously-measured beam squint. The two methods gave comparable results, which shows that one can, indeed, apply measured beam squint and squash to measured angular derivatives of H I emission to derive – and subtract out – the instrumental contribution.

Averaging over all 24 hours zeros out the contributions from beam squint and squash, because their structure in the azimuthal direction around beam center averages to zero. It also eliminates some, and probably nearly all, of the sidelobe contributions. For the average of all RAs the V spectrum is an excellent fit to the derivative of the I spectrum, with $B_{\parallel} = 8.8 \pm 0.4 \mu\text{G}$ (Heiles 1996b); this is in excellent agreement with the measurements nearby in the sky (Heiles 1989). He also found a systematic variation of B_{\parallel} with RA from ~ 7 to $12 \mu\text{G}$, indicating the contribution of instrumental errors. The amplitude of the first Fourier component $\sim 2.0 \mu\text{G}$ and of the second $\sim 0.58 \mu\text{G}$. The

additional uncertainty produced by this variation, calculated as an r.m.s., is $1.4 \mu\text{G}$. The first Fourier component is significantly higher than the others, while the second is comparable to them and is probably not significant with respect to noise.

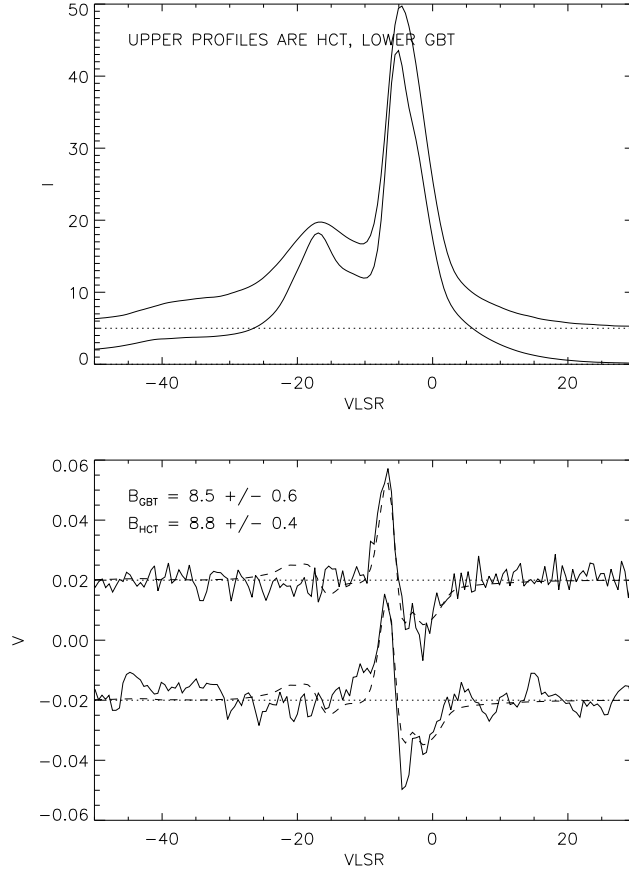


Fig. 6. Stokes I (top) and V (bottom) for H I emission towards the NCP for two telescopes, the HCRO and the GBT. The upper profile in each panel is from HCRO.

Heiles et al. (2003) have performed a similar analysis of the North Celestial Pole using the Green Bank Telescope. The analysis is not yet complete because the data were taken recently. Nevertheless, the 24-hour average for the GBT is in excellent agreement with the above HCRO results, yielding $B_{\parallel} = 8.5 \pm 0.8 \mu\text{G}$. Figure 6 compares the results for the two telescopes; recall that the

beam areas differ by a factor of 16! If anything, sidelobe effects in the line wings seem higher for the GBT spectrum.

Most of the published HCRO results did not, in fact, go through the procedure of subtracting out the instrumental contribution. Rather, any position having a significant instrumental contribution, i.e. one that exceeded about one third of the measured results, was not published. Quoted errors on the published results do not include the instrumental contribution, so they are too small; a conservative estimate of the instrumental error in quoted results depends on circumstances, but is typically of order 30% of the derived value. This is relatively high, and a few quoted values may be incorrect and even of the wrong sign. Nevertheless, the published results should be relatively reliable given these caveats.

All this means that HCRO reliably measured strong fields in H I emission, but not weak fields. Thus, those measurements cannot be used statistically, as the absorption measurements of Sect. 4 can be.

5.4 Overview of the HCRO H I Emission Results

The HCRO telescope was devoted almost exclusively to Zeeman splitting during the years before its catastrophic demise in 1993 (Heiles 1993). It made many Zeeman splitting detections in H I emission. Figure 7 shows a global map of these detections, which are presented in five publications (Heiles 1988, 1989, Goodman & Heiles 1994, Myers et al. 1995, Heiles 1997). Below we present the briefest of brief summaries of each.

- Heiles (1988) mapped $B_{||}$ for 27 positions in the vicinity of the filamentary dark cloud L204, detecting Zeeman splitting in H I emission for all 27 and also H I self-absorption for 12 positions. This remains the best $B_{||}$ -mapped example of a well-defined, isolated dark cloud. The $B_{||}$ exhibits correlation with starlight polarization, CO velocities V_{CO} , and the shape of the curvy filament, implying that projection effects are responsible for much of the structure and allowing an estimate $B_{tot} = 12 \mu\text{G}$. The field dominates ram pressure from systematic flows and also dominates the self-gravity of the molecular gas. This cloud seems worth further study because it is well-defined with interesting correlations, and would benefit from redoing the correlations with better angular resolutions.
- Heiles (1989) mapped $B_{||}$ in a number of morphologically obvious regions, meaning high-contrast filaments. These included several supernova or superbubble shells such as Eridanus, the North Polar Spur, and the North Celestial Pole Loop. In every morphologically obvious structure, the fields were strong ($|B_{||}| \gtrsim 5 \mu\text{G}$) and the field retained the same sign over the feature. Magnetic pressure overwhelmingly dominates thermal pressure, and it even dominates turbulent pressure. The paper considers the filaments to be true filaments instead of edge-on sheets, but we wonder if this is correct; this is an important question and needs to be resolved. If the

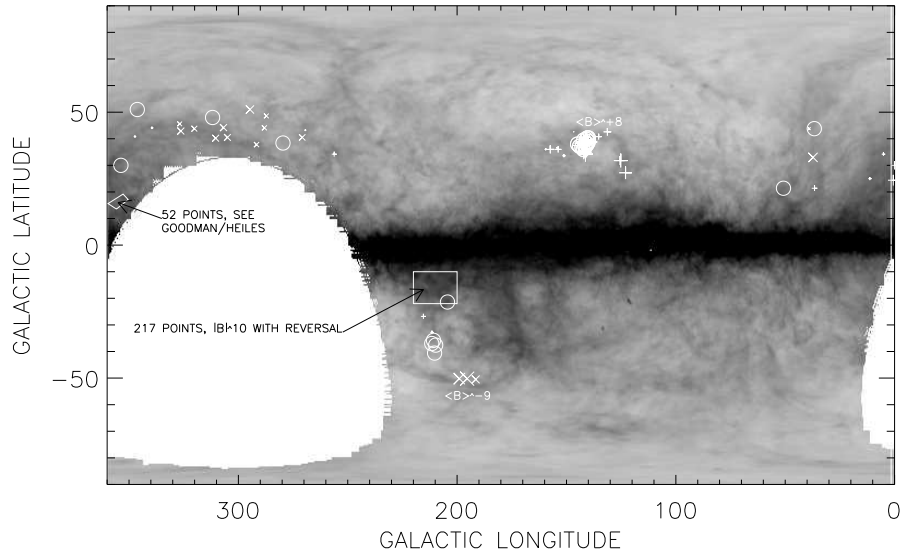


Fig. 7. Detections of magnetic fields in emission from Heiles (1988, 1989), Goodman & Heiles (1994), Myers et al. (1995) and Heiles (1997), superposed on a map of H I in which blacker means more H I.

structures are edge-on sheets, then the observed values $|B_{\parallel}| \gtrsim 5 \mu\text{G}$ imply $B_{\text{tot}} \sim 10 \mu\text{G}$ from our discussion in Sect. 3.4, meaning that the field is mildly amplified in old supernova shocks.

- Goodman & Heiles (1994) mapped B_{\parallel} for 52 positions in Ophiuchus, detecting it for 43 Gaussian components in 29 positions. 16 of the 43 components were in self-absorption having the same velocity as, and therefore associated with, molecular gas. Combining the Zeeman-splitting results with optical polarization data allows them to determine not only B_{\parallel} but also B_{\perp} and, consequently, B_{tot} ; it is $10.6 \mu\text{G}$, with the field inclined to the line of sight by 32° . About half the magnetic energy is associated with the random field component, and the magnetic and kinetic energy densities are comparable.
- Myers et al. (1995) detected B_{\parallel} for 1 position in the Draco dark cloud and 31 positions in the Ursa Major (North Celestial Pole) loop. Magnetic and kinetic energy densities are comparable.

One HCRO detection, at $(\ell, b) = (141^{\circ}1, 38^{\circ}8)$, is remarkably strong, with $B_{\parallel} = 18.9 \pm 1.8 \mu\text{G}$. However, the same position observed with the Effelsberg 100-m telescopes yields the completely discrepant $B_{\parallel} = 3.5 \pm 3.7 \mu\text{G}$. This is a real problem and not simply a difficulty with one of the telescopes, because two other HCRO positions observed with Effelsberg yielded consistent results. Given the factor 16 difference in beam area, it would seem that there is much angular structure in B_{\parallel} at this position! But this needs to be checked by mapping the locale with, say, the GBT.

- Heiles (1997) mapped B_{\parallel} for 217 positions covering $\sim 100 \text{ deg}^2$ in the Orion/Eridanus loop region. The goal was to develop a holistic interpretation of the magnetic field structure on small and large size scales. The observations were interpreted as a large-scale ambient field distorted by the superbubble's shock, together with smaller-scale structure produced by local perturbations. But the match to the data is sketchy and vague, at least in part because of the geometrical situation described in the next paragraph, so the goal was realized only in part. Nearly all of the area mapped is permeated by a negative field (pointing towards the observer); a small ($\sim 10 \text{ deg}^2$) region has a uniformly positive field, which is associated with a unique velocity component, different from those associated with the negative field. The reversal in sign had been previously interpreted as a toroidal field, but this may not be correct because of the different velocity components; an alternative interpretation involves field lines wrapped around a molecular filament by the shock front produced by the superbubble explosions.

As part of the analysis, Heiles (1997) develops a simple geometrical model of field lines distorted by the Eridanus superbubble shock front. For individuals who are interested in studying the magnetic field perturbations produced by shocks, this model is worth some study as an illustrative example of the general case. The patterns of B_{\perp} and B_{\parallel} , revealed by observations of starlight polarization and of Zeeman splitting, are very complicated, more than one naively imagines. They depend, firstly, on the direction of the ambient field relative to the line of sight. They also depend on the position within the structure. Most importantly, they also depend on which wall of the superbubble – the near or the far wall – produces most of the extinction or H I column density. The North Polar Spur, with its easily recognizable starlight polarization effect, is a very unusual and deceptively simple case because we see the ambient field nearly in the plane of the sky.

6 Importance of Magnetic Fields in Molecular Clouds

Here we will both review the observational data and focus on one of the main reasons for observing magnetic fields in molecular clouds – to try to understand their role in the evolution of dense clouds and in the star formation process. Understanding star formation is one of the outstanding challenges of modern astrophysics. However, in spite of significant progress in recent years, there remain unanswered fundamental questions about the basic physics of star formation. In particular, what drives the star formation process? The prevailing view has been that self-gravitating clouds are supported against collapse by magnetic fields, with ambipolar diffusion reducing support in cores and hence driving star formation (e.g., Mouschovias and Ciolek 1999). The other extreme is that molecular clouds are intermittent phenomena in an inter-

stellar medium dominated by turbulence, and the problem of cloud support for long time periods is irrelevant (e.g., Elmegreen 2000). In this paradigm, clouds form and disperse by the operation of compressible turbulence (Mac Low and Klessen 2004), with clumps sometimes becoming gravitationally bound. Turbulence then dissipates rapidly, and the cores collapse to form stars. Hence, there are two competing models for driving the star formation process. The fundamental issue of what drives star formation is far from settled, on either observational or theoretical grounds. Since the main difference between the two star-formation scenarios listed above is the role of magnetic fields, observations of magnetic fields in star formation regions are crucial.

Observations of magnetic fields in molecular clouds have now become a fairly routine procedure. Great progress has been made in mapping polarized emission from dust, and the first detections of linearly polarized spectral lines have been made. Only the Zeeman technique has been used for both diffuse H I and dense molecular clouds. Measuring Zeeman splitting in molecular clouds is both easier and harder than in the H I. Instrumental effects are less important because the sources are confined in angle so that polarized sidelobes often lie off of the source; this makes it easier. However, molecular lines are typically much weaker than the H I line, the frequencies are all higher, and the Landé g factors are somewhat smaller; although this makes it harder, there is compensation in the form of narrower line widths and higher field strengths in the denser molecular clouds. So progress in molecular Zeeman measurements has been possible.

7 Molecular Cloud Observational Results

There has been a remarkable explosion in the observational data on magnetic fields in molecular clouds in the last few years. Hildebrand and collaborators have mapped warm molecular clouds in the far infrared; that work is reviewed by Hildebrand (2002, 2003). The JCMT SCUBA polarimeter has been used by multiple investigators (Matthews et al. 2001; Chrysostomou et al. 2002; Wolf et al. 2003; Crutcher et al. 2004) to map polarized dust emission at $850\ \mu\text{m}$ in both warm clouds and cool cores. The BIMA millimeter array has been used to map linearly polarized dust and spectral line emission at 3 and 1.3 mm at $2'' - 6''$ resolution (Lai et al. 2003). Crutcher (1999) reviewed all molecular Zeeman observations made at that time and analyzed in detail the 15 positive detections. Since then, two major surveys of OH Zeeman have been carried out (Bourke et al. 2001; Troland and Crutcher 2004) that have added to the total. Finally, Zeeman measurements in OH (Fish et al. 2003; Caswell 2003, 2004) and H₂O (Sarma et al. 2002) masers, which probably probe magnetic fields in shocked molecular regions, have been made. See references to additional results in the above papers.

Space precludes discussion of all the results. Instead, we discuss magnetic field results for a small number of molecular clouds, chosen to illustrate the

range of the data available and the astrophysical conclusions that may be inferred. These are a starless, low-mass core (L 183), a region of low-mass star formation with a CO bipolar outflow (NGC 1333 IRAS4A), a region with evidence of high-mass star formation but no H II region (DR 21 OH), and a region with high-mass star formation and an H II region (S 106).

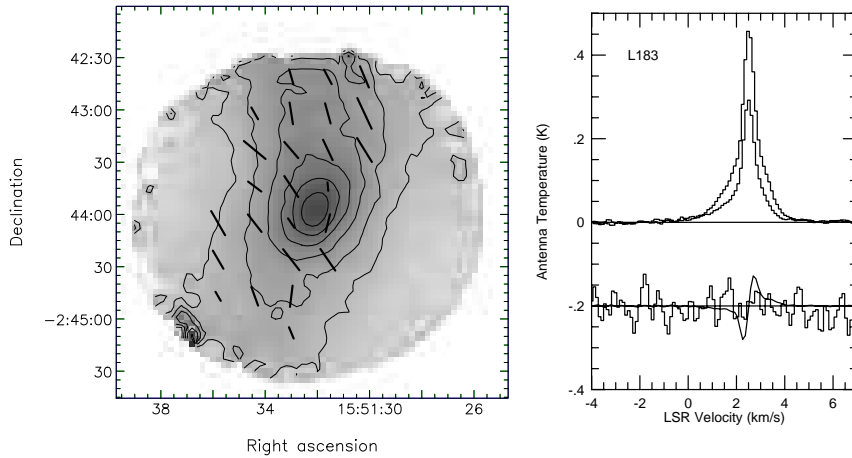


Fig. 8. Left: Dust polarization map of the starless core L 183. Grey-scale and contours show the dust emission at $850 \mu\text{m}$. Thick line segments show the direction of the magnetic field projected on the sky; lengths are proportional to the polarized flux. Right: OH 1665 and 1667 MHz line profiles toward L 183. Observed data are histogram plots; the fit to Stokes V in the lower panel is a line. Top panel shows the two Stokes I spectra. Bottom panel shows the mean Stokes V spectrum for the two lines with a $3\text{-}\sigma$ upper limit fit.

7.1 The Starless Core L 183

L 183 is a dark cloud that contains a starless core – a dense concentration of a few solar masses with no evidence that a protostar or star has yet formed. Figure 8 shows observational results for the magnetic field; the left panel shows the SCUBA dust emission and polarization map at $850 \mu\text{m}$ (Crutcher et al. 2004), while the right panel shows the NRAO 43-m telescope observation of Stokes I and V spectra of 18-cm OH lines (Crutcher et al. 1993). The dust polarization map has an angular resolution of $21''$ and covers $3'$; the observed dust polarization position angles have been rotated by 90° so the line segments are in the direction of B_\perp . The OH spectra were obtained with a telescope beam diameter of $18'$.

The dust polarization map samples the core of L 183, with a density of $n(\text{H}_2) \approx 3 \times 10^5 \text{ cm}^{-3}$. The magnetic field is fairly regular, in agreement with

the field being strong enough to resist turbulent twisting. But the dispersion in position angles of 14° is significant, implying that some turbulent twisting is present. The angle between the projected minor axis of the core and the mean direction of B_\perp is $\sim 30^\circ$. Applying the Chandrasekhar-Fermi technique yields $B_\perp \approx 80 \mu\text{G}$. The OH Zeeman spectra sample a much larger area – the extended envelope of the L 183 core, for which $n(\text{H}_2) \approx 1 \times 10^3 \text{ cm}^3$. The Zeeman effect is not detected to a 3- σ upper limit of $B_\parallel < 16 \mu\text{G}$.

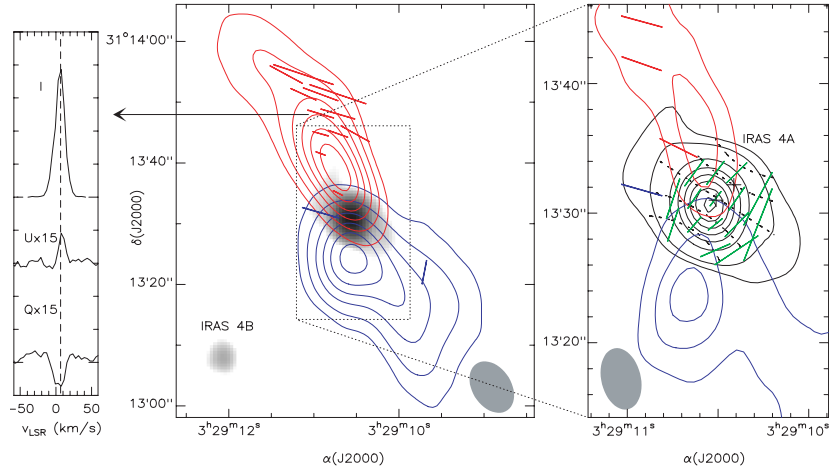


Fig. 9. BIMA observations of NGC 1333 IRAS4A. The middle panel shows dust emission (greyscale) and CO 2-1 emission from the bipolar outflow (contours). Line segments superposed on the outflow show the polarization of the line emission. The mean Stokes I, U, and Q profiles for the northern lobe are shown in the left panel. The right panel shows the central region dust emission (thick contours), CO outflow (thin contours), CO polarization (black line segments), and dust polarization (grey line segments). Dotted lines show a possible hourglass morphology for **B**.

7.2 NGC 1333 IRAS4A

NGC 1333 IRAS4A is a later stage in star formation than L 183 – a very young low-mass star formation region with multiple young stellar systems and an associated molecular outflow. Figure 9 shows BIMA observations (Girart, Crutcher, and Rao 1999) of the dust and CO outflow emission and polarization at 1.3 mm. The line polarization is perpendicular to the dust polarization. In the outflow, where the direction of the velocity gradient is known, it is possible to predict theoretically (Kylafis 1983) that the line polarization should be parallel to B_\perp and therefore perpendicular to the dust polarization, as observed. The outflow is initially north-south, at about a 50° angle to B_\perp . A successful theory of molecular outflows must account for such a difference between **B**

and the outflow. However, about $25''$ from the center the difference is only 15° , suggesting that the field has deflected the outflow. The morphology of the dust polarization is again smooth and suggestive of a pinched or hourglass morphology.

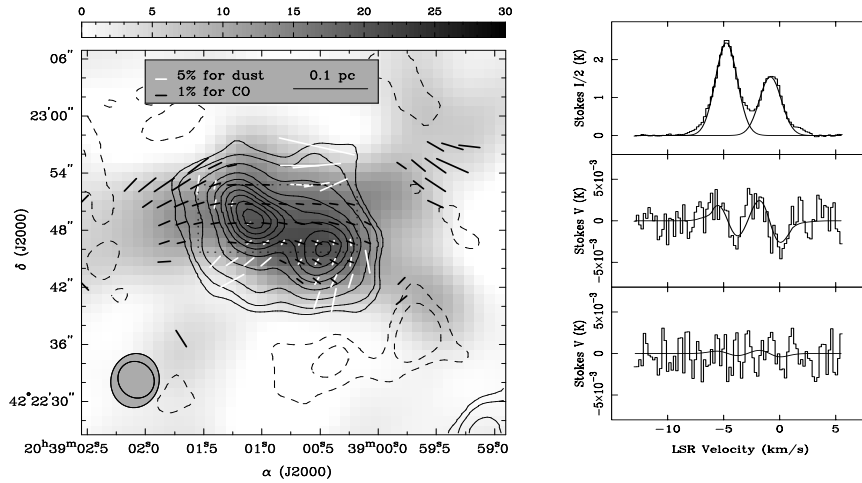


Fig. 10. Left: BIMA map of the high-mass star formation region DR 21 (OH). Contours show the 1.3-mm dust emission, grey scale shows the CO 2-1 line emission integrated over velocity, white line segments show the dust polarization, and black line segments show the CO linear polarization. Right: CN 1-0 line profiles toward DR 21 (OH). Observed data are histogram plots, fits are lines. Top panel shows the Stokes I spectrum with two Gaussians fitted. Middle panel shows the mean Stokes V spectrum for the four hyperfine components that have strong Zeeman splitting coefficients Z ; the bottom panel shows the three components with weak Z . $B_{||}$ was fitted independently for the two Gaussian lines. The fields derived from these data are $B_{||} = -0.4 \pm 0.1$ mG and $B_{||} = -0.7 \pm 0.1$ mG for the velocity components at -4.7 km s $^{-1}$ and -1.0 km s $^{-1}$, respectively.

7.3 DR 21 (OH)

Figure 10 shows results for the high-mass star formation region DR 21 (OH); the left panel shows the BIMA dust and CO emission and polarization map at 1.3 mm (Lai, Girart, and Crutcher 2003), while the right panel shows IRAM 30-m telescope Stokes I and V spectra of the 3-mm CN lines (Crutcher et al. 1999). In millimeter-wave dust emission the main component of DR 21 (OH) consists of two compact cores (Woody et al. 1989) with a total mass of $\sim 100 M_{\odot}$. The two CN velocity components are each centered on a different one of the two compact cores. The region has associated masers of OH (Norris et al. 1982), H_2O (Genzel and Downes 1977), and CH_3OH (Batra and Menten

1988), and high-velocity outflows powered by the two compact cores (Lai, Girart, and Crutcher 2003). The results from the dust and CO 2-1 linear polarization maps suggest that the magnetic field direction in DR 21 (OH) is parallel to the CO polarization and therefore parallel to the major axis of DR 21 (OH). This could be explained by a toroidal field produced by rotation of the double core. The strong correlation between the CO and dust polarization suggests that magnetic fields are remarkably uniform throughout the envelope and the cores. Both the dust emission and the CN lines sample a density $n(H_2) \approx 1 \times 10^6 \text{ cm}^3$. The Chandrasekhar-Fermi technique yields $B_\perp \approx 1 \text{ mG}$, compared with $B_\parallel = -0.4 \pm 0.1 \text{ mG}$ and $B_\parallel = -0.7 \pm 0.1 \text{ mG}$ inferred from the CN Zeeman detections shown in figure 10. Combining these results, the total field strength $B_{\text{tot}} \approx 1.1 \text{ mG}$ and \mathbf{B} is at an angle $\theta \sim 60^\circ$ to the line of sight. However, uncertainties in B_\perp and in B_\parallel are sufficiently large that θ is quite uncertain.

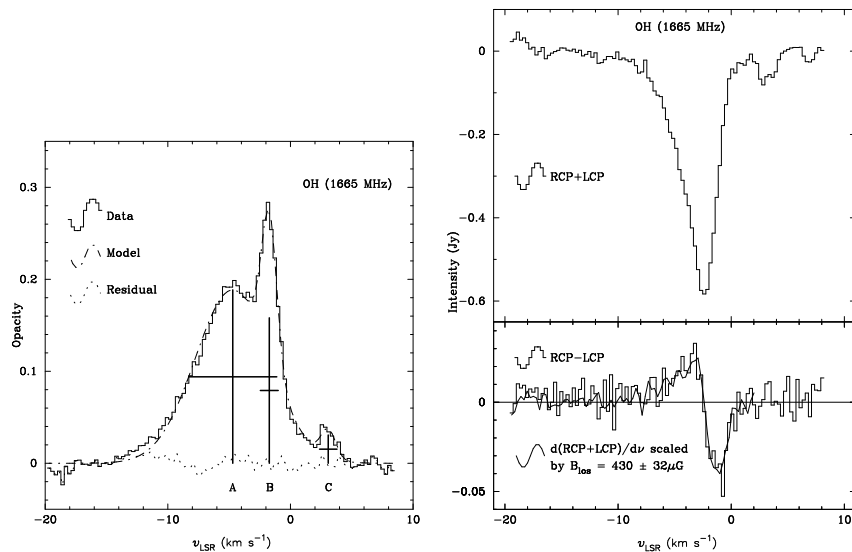


Fig. 11. Left: Optical depth profile for the 1665 MHz line toward S106. Right: Stokes I and V spectra toward the position of maximum B_\parallel toward S106.

7.4 S 106

S 106 is a bipolar H II region $\sim 0.5 \text{ pc}$ in length embedded in an $\sim 4 \text{ pc}$ diameter molecular cloud with $\bar{n}(H_2) \approx 1.4 \times 10^3 \text{ cm}^{-3}$ and $M \approx 2000 M_\odot$ (Schneider et al. 2002). Roberts et al. (1995) mapped B_\parallel in OH absorption lines with the VLA. Figure 11 shows the line optical depth profile, to which

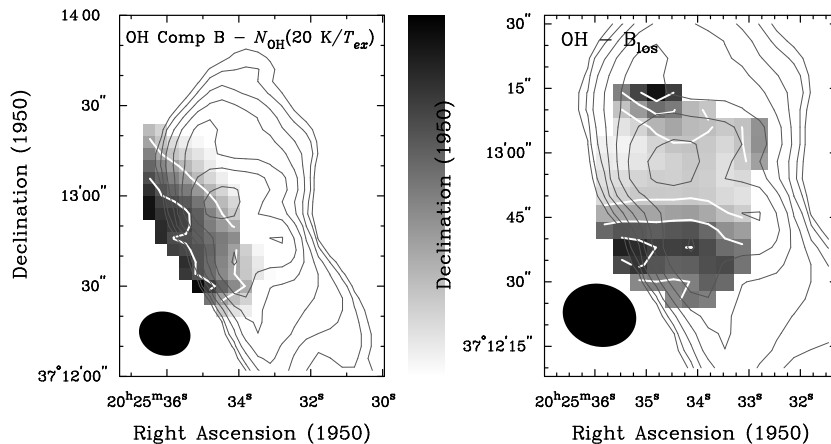


Fig. 12. Left: Map of $N(\text{OH})$ for the narrow “B” line component toward S106. For $T_{ex} = 50$ K (Schneider et al. 2002), contours are 1 and 2×10^{15} cm^{-2} . Right: Map of $B_{||}$ toward S106. Contours are at 200, 300, and 400 μG .

three Gaussian components have been fit. Component B is a narrow component that corresponds with the CO emission seen over the entire molecular cloud; this is gas undisturbed by the H II region. The broader component A arises in gas that has been shocked by the expansion of the H II region. The Zeeman effect is seen (Fig. 11) in component B, so the $B_{||}$ map is of the undisturbed molecular gas and not material that has been compressed into a shell surrounding the H II region. Figure 12 shows maps of $N(\text{OH})$ and $B_{||}$. The component B gas has a strong peak to the east of the H II region, which is seen as a high-density clump in the molecular emission line maps; Schneider et al. (2002) find $N(\text{H}_2) \approx 3 \times 10^{22}$ cm^{-2} for this clump.

7.5 Maser Zeeman Observations

OH masers are found associated with the early stage of massive star formation, with maser spots coming from the dense ($\sim 10^7$ cm^{-3}) molecular envelope surrounding the massive star. Because of their brightness, they serve as signposts identifying sites of recently formed massive stars, and can be used to study kinematic and physical conditions in the dense molecular material. The ground state $^2\Pi_{3/2}$, $J = 3/2$ OH masers sometimes have clearly identifiable Zeeman pairs, that imply milligauss magnetic field strengths. Here B_{tot} is measured since the two Zeeman pairs are (generally) separated. Argon et al. (2000) surveyed 91 regions with the VLA A-array in both senses of circular polarization simultaneously, in order to identify Zeeman pairs.

Fish et al. (2003) analyzed this sample and found more than 100 Zeeman pairs in more than 50 regions. Field strengths range from ~ 0.1 mG to ~ 10 mG. They derived a magnetic field direction for each massive star formation

region and looked for correlations, such as the correlations between maser field directions and the large-scale Galactic field suggested by Davies (1974) based on a much smaller data set. The more complete data did not show this correlation, which if present would have required a preservation in field direction between the very diffuse and the very dense gas.

Excited state OH (${}^2\Pi_{3/2}$, $J = 5/2$ and $J = 7/2$) maser lines were observed by Caswell (2003, 2004). The excited-state masers tend to have fewer components and “cleaner” Zeeman pairs than the ground-state masers. Field strengths are similar to those found in the ground-state maser lines.

Fiebig & Güsten (1989) detected Zeeman splitting in the ($6_{16} - 5_{23}$) H₂O maser lines toward W 3, Orion KL, W49N, and S140 and inferred field strengths up to 50 mG. H₂O masers probe densities $\sim 10^{8-9}$ cm⁻³. Because H₂O does not have an unpaired electron, the Zeeman splitting is proportional to the nuclear magneton, and only B_{\parallel} could be measured. Sarma et al. (2002) used the VLA to continue these studies, finding $B_{\parallel} \approx 13 - 49$ mG in four massive star formation regions. They argued that the masers arise in C-shock regions, and that the magnetic and turbulent energies are close to equilibrium. Sarma et al. (2001) used the VLBA to map four H₂O maser spots in W3 IRS5, finding that B_{\parallel} varied by a factor of three over 150 au but did not change sign. This might be expected if the masers and magnetic field are entrained in a coherent outflow.

8 Model Predictions and Observational Tests

Crutcher’s (1999) review of the molecular Zeeman-splitting measurements available at that time included a detailed discussion of physical conditions and an astrophysical discussion of the implications of the data. He found that magnetic fields play an important role in molecular clouds, as they do in the diffuse H I reviewed above. Typically $\beta_{\text{th}} \sim 0.04$ and $\beta_{\text{turb}} \sim 1$, so the turbulent and magnetic energy densities are comparable. He also discussed the “mass to magnetic flux” ratio and the scaling of B_{\parallel} with density ρ . These topics will be considered in more detail below.

8.1 Mass-to-Flux Ratio

In contrast to the diffuse H I, gravity plays an important role in molecular clouds. From the virial theorem and assuming flux freezing, one can straightforwardly derive the result that the ratio of gravitational to magnetic energy is independent of size. This, in turn, means that the relative importance of gravity and magnetism is maintained. This relative importance is measured by the “mass to magnetic flux” ratio M/Φ , which is proportional to the ratio N_{\perp}/B_{tot} (where N_{\perp} is the column density perpendicular to the sheet or disk of matter, i.e., along the magnetic field direction for a magnetically supported

cloud). We use the symbol $\mu_{\text{intrinsic}}$ to denote M/Φ in units of the critical value for a slab, $\mu_{\text{intrinsic}} = (2\pi G^{1/2})^{-1}$ (Nakano & Nakamura 1978). Then

$$\mu_{\text{intrinsic}} = 7.6 \times 10^{-21} \frac{N_{\perp}(H_2)}{B_{\text{tot}}}. \quad (22)$$

In the ambipolar diffusion model clouds are initially subcritical, $\mu_{\text{intrinsic}} < 1$. Ambipolar diffusion is fastest in shielded, high-density cores, so cores become supercritical, and rapid collapse ensues. The envelope continues to be supported by the magnetic field. Hence, the prediction is that $\mu_{\text{intrinsic}}$ must be < 1 in cloud envelopes, while in collapsing cores $\mu_{\text{intrinsic}}$ becomes slightly > 1 . Hence, this model tightly constrains $\mu_{\text{intrinsic}}$. On the other hand, the turbulent model imposes no direct constraints on $\mu_{\text{intrinsic}}$, although strong magnetic fields would resist the formation of gravitationally bound clouds by compressible turbulence. Also, if magnetic support is to be insufficient to prevent collapse of self-gravitating clumps that are formed by compressible turbulence, the field must be supercritical, $\mu_{\text{intrinsic}} > 1$. $\mu_{\text{intrinsic}}$ may take any value > 1 , although of course for turbulence models that happen to have weak magnetic fields, clouds will be highly supercritical, $\mu_{\text{intrinsic}} \gg 1$ (Mac Low & Klessen 2004).

If B_{tot} is strong, clouds will have a disk morphology with \mathbf{B} along the minor axis. To properly measure $\mu_{\text{intrinsic}}$, one needs B and N along a flux tube, i.e., B_{tot} and N_{\perp} . We use our discussion in Sect. 3.4 to relate μ_{obs} to $\mu_{\text{intrinsic}}$, which is $\propto N_{\perp}/B_{\text{tot}}$. For a randomly oriented assembly of sheets all having the same N_{\perp} , the median N_{obs} is $2N_{\perp}$. For a randomly oriented set of uniformly strong magnetic fields, the median $B_{\parallel} = B_{\text{tot}}/2$. Thus, the median value of the ratio $N_{\text{obs}}/B_{\parallel}$ is $4N_{\perp}/B_{\text{tot}}$. However, it may be more appropriate to use the mean rather than the median value:

$$\left\langle \frac{M}{\Phi} \right\rangle = \int_0^{\pi/2} \frac{M_{\text{obs}} \cos \theta}{\Phi_{\text{obs}} / \cos \theta} \sin \theta d\theta = \int_0^{\pi/2} \left(\frac{M}{\Phi} \right)_{\text{obs}} \cos^2 \theta \sin \theta d\theta = \frac{1}{3} \left\langle \frac{M}{\Phi} \right\rangle_{\text{obs}}. \quad (23)$$

Thus, the mean value of the observed ratio is three times the intrinsic ratio, i.e. $\langle N_{\text{obs}}/B_{\parallel} \rangle = 3\langle N_{\perp}/B_{\text{tot}} \rangle$.

Crutcher (1999) listed values of $\mu_{\text{obs}} \propto N_{\text{obs}}/2B_{\parallel}$, which are derived from observed values instead of the intrinsic ones N_{\perp} and B_{tot} . He included the factor of 2 for the magnetic field, but not the additional correction factor for the column density. He noted that such a correction would be necessary for magnetically supported clouds that would have a disk morphology, but preferred not to apply an additional geometry factor since the morphology of the molecular clouds was not known directly from the observations. However, the prediction of the magnetic support model is a disk morphology, so one must apply the column density correction to test this model.

Crutcher reported the median $\mu_{\text{obs},1/2} = 2.2 \pm 0.3$. We conclude that for that sample of molecular clouds, the intrinsic and observed μ are related

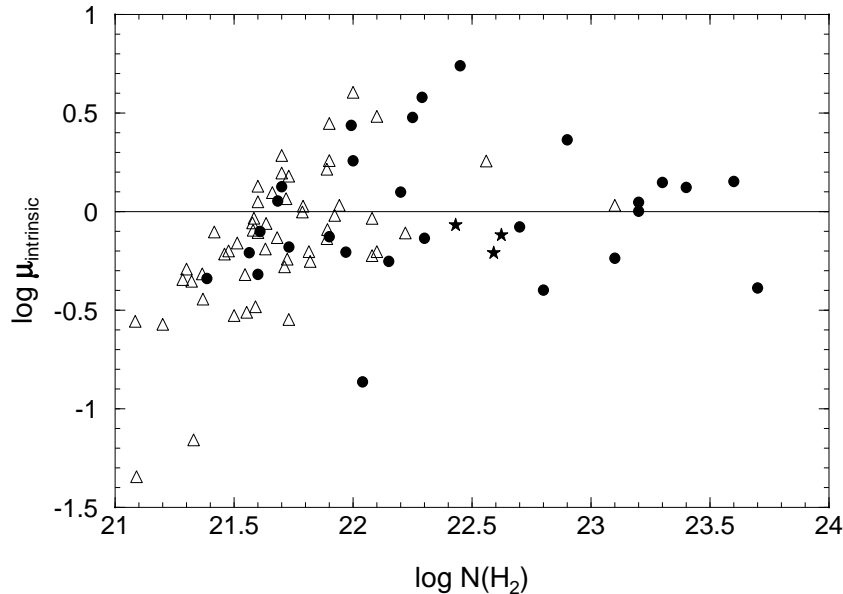


Fig. 13. $\mu_{intrinsic}$ are the observed mass to magnetic flux ratios, divided by 3 to correct for projection bias, in units of the critical values. $\mu_{intrinsic} > 1$ is supercritical, $\mu_{intrinsic} < 1$ is subcritical. Dots are for Zeeman data with $B_{||} > 3\sigma(B_{||})$, stars are for Chandrasekhar-Fermi estimates of B_{\perp} , and triangles are lower limits plotted at $B_{||} = 3\sigma(B_{||})$. Although the statistical correction of $1/3$ for geometrical bias has been applied to each point, so that statistically this plot should be valid, for any individual point the true μ could be higher or lower than the plotted $\mu_{intrinsic}$. Some of the scatter is therefore still due to geometrical projection effects.

by $\mu_{intrinsic,1/2} = \mu_{obs,1/2}/2$ if we choose the median and by $\mu_{intrinsic} = \mu_{obs,1/2}/1.5$ for the mean. Therefore, $\mu_{intrinsic,1/2} \sim 1.1$ (median) or 1.5 (mean). This puts these clouds into the regime in which magnetism is closely comparable to gravity. Presumably they are in general not currently suffering gravitational collapse, because they appear to be stable entities. (Once a core becomes supercritical, the time scale for collapse is very short, so few cores can be at this stage.) They are on the verge of becoming supercritical: in the absence of external perturbations, they will gradually evolve by ambipolar diffusion to the point where gravitational collapse can occur. Estimates of μ_{obs} for additional clouds may be obtained from the OH Zeeman surveys of Bourke et al. (2001) and Troland and Crutcher (2004), and from estimates of B_{\perp} with the Chandrasekhar-Fermi method applied to linear polarization maps of cores (Crutcher et al. 2004). Figure 13 shows all of the $\mu_{intrinsic}$ now available, where the mean value correction of $1/3$ has been used. That is, the plotted $\mu_{intrinsic} = \mu_{obs}/3$. The observations are distributed roughly equally above and below the $\mu_{intrinsic} = 1$ line that divides subcritical and

supercritical M/Φ ratios for disk geometries. Therefore, the data suggest that $\bar{\mu}_{intrinsic} \approx 1$; that is, the typical mass to magnetic flux ratio is approximately critical. There is a slight indication that for large column densities, $\bar{\mu}_{intrinsic}$ may be supercritical, and for small column densities, subcritical.

It is also relevant to consider mass-to-flux ratios in H I clouds, from which molecular clouds presumably form. Results from the Arecibo Millennium Survey showed that for all of the detections, the μ_{obs} were significantly subcritical. Moreover, almost all of the non-detections were also consistent with $\mu_{obs} < 1$. If these points were to be plotted on Figure 13, they would lie to the left of and below the $\mu_{intrinsic} = 1$ line. Hence, the H I data suggest that the precursors to molecular clouds are subcritical, as required by the magnetic support model.

In the ambipolar diffusion model the envelopes of dark clouds are the regions where M/Φ remains essentially unchanged while ambipolar diffusion drives M/Φ supercritical in the core. Hence, envelopes of dark clouds provide a crucial test of magnetic support models – M/Φ *must* be subcritical in these regions. Observations of dark-cloud cores were carried out by Crutcher et al. (1993), but the 18' telescope beam size meant that the cores occupied a small fraction of the beam; mainly, the envelope regions were sampled. The result was $\bar{\mu}_{intrinsic} \gtrsim 1$, rather than the $\mu_{intrinsic} < 1$ required by magnetic support. However, the geometrical correction to the column density was not applied; with this correction, $\bar{\mu}_{intrinsic}$ would be slightly subcritical, as required by the magnetic support model.

8.2 Scaling

The scaling of B_{tot} with density ρ is usually parameterized as $B_{tot} \propto \rho^\kappa$, so our discussion will be in terms of κ . For strong magnetic fields, a cloud may be supported perpendicular to the field, but the field provides no support along the field. Then clouds will be disks rather than spheres. With the assumption that self-gravity is balanced only by internal thermal pressure along the symmetry axis z , $2\pi G\rho z^2 = c^2$ (this expression was derived for the plane-parallel or infinite thin disk case and first applied in astrophysics by Spitzer (1942) to the structure of the Galaxy perpendicular to the plane). Then the expression for magnetic flux freezing ($\frac{M}{\Phi} \propto 2\pi\rho R^2 z / \pi R^2 B$) makes it possible to eliminate z from Spitzer's expression, yielding $B \propto \sqrt{\rho T}$. For an isothermal core, $\kappa = 1/2$. Detailed calculations of the evolution of a cloud collapsing due to ambipolar diffusion show that since the ambipolar diffusion timescale is much shorter in a core than in an envelope, the core will become supercritical and collapse while the envelope remains subcritical and supported by the field. Hence, B_{tot} in cloud envelopes remains virtually unchanged, so at lower densities no strong correlation between B_{tot} and density ρ is predicted, and $\kappa \sim 0$. As ambipolar diffusion increases M/Φ in a core, ρ increases faster than B_{tot} and κ increases rapidly. After the core becomes supercritical, it will col-

lapse much more rapidly than the ambipolar diffusion rate, and κ continues to increase and approaches a limit of 0.5 (Ciolek & Basu 2000).

Once a self-gravitating clump is formed by turbulence, if gravity exceeds both turbulent and magnetic support, the clump will collapse rapidly, at near the free-fall rate. Mestel & Spitzer (1956) considered the case of a spherically contracting cloud, for which the magnetic field was too weak to affect the collapse morphology; they showed that $\kappa = 2/3$ for this case. Hence, this would be the prediction for a core formed by turbulence with no significant magnetic support against gravity. On the other hand, if virial equilibrium is achieved between gravity and turbulence ($3GM^2/5R = 3M\sigma^2/2$), then $\rho R^2 \propto \sigma^2$. Flux freezing ($M \propto \Phi$) gives $\rho R \propto B_{\text{tot}}$, so $B_{\text{tot}} \propto \sigma \rho^{1/2}$ is predicted.

Determining κ observationally can distinguish between the various scenarios. $\kappa = 2/3$ implies a collapsing core with no significant magnetic or kinetic support. $\kappa < 0.5$ suggests a magnetically supported cloud, with $\kappa \rightarrow 0.5$ as M/Φ goes from subcritical to supercritical. Finally, $\kappa = 1/2$ but with an additional scaling of B_{tot} with the turbulent velocity dispersion σ is predicted for a core in virial equilibrium, with magnetic fields and turbulence (or thermal motions) providing support.

At low densities $n \sim 0.1 - 100 \text{ cm}^{-3}$, it has been clear for some time that there is no correlation of B_{tot} with ρ (Troland and Heiles 1986). Crutcher's analysis of the higher density, molecular cloud data used the observed parameters N_{obs} and B_{\parallel} (not the intrinsic ones N_{\perp} and B_{tot}). A least squares fit showed that $\log B_{\parallel} \propto [\log n(H_2)]^{0.47}$, which is consistent with ambipolar diffusion driven contraction of clouds (Fiedler & Mouschovias 1993) or, alternatively, with a constant Alfvénic Mach number M_{ALF} .

One year later, Basu (2000) extended Crutcher's analysis by including the velocity dispersion in the correlation. For slablike clouds, the combination of hydrostatic pressure equilibrium and the mass to flux ratio yields the expected relationship from Basu's equation (3),

$$B_{\text{tot}} = (8\pi)^{1/2} \sigma_v \rho^{1/2} \frac{c_1^{1/2}}{\mu_{\text{intrinsic}}} \quad (24)$$

where σ_v is the velocity dispersion and ρ the mean mass density across the slab. The parameter c_1 relates the midplane volume density to the mean density ($c_1 \geq 1$). Basu replotted Crutcher's points, with the remarkable result shown in Fig. 14: the rms scatter in $\log B_{\parallel}$ dropped by nearly a factor of two, from Crutcher's fit with $\Delta(\log B_{\parallel}) \sim 0.40$, to Basu's with $\Delta(\log B_{\parallel}) \sim 0.23$. The data and Basu's fit are shown in Fig. 14 as the diamonds and solid line. The dashed line is the theoretical prediction from (24) for $c_1^{1/2}/\mu_{\text{intrinsic}} = 1$, which is parallel to and just little larger than the solid-line fit to the data.

The logarithmic rms dispersion $\Delta(\log B_{\parallel}) \sim 0.23$ is remarkably small. This corresponds to dispersion of a factor of only 1.7 in magnetic field B_{\parallel} ; alternatively, because the slope is one, it also corresponds to a factor 1.7 in $\sigma_v n^{1/2}$. We expect large variations in B_{\parallel} because of the projection factor

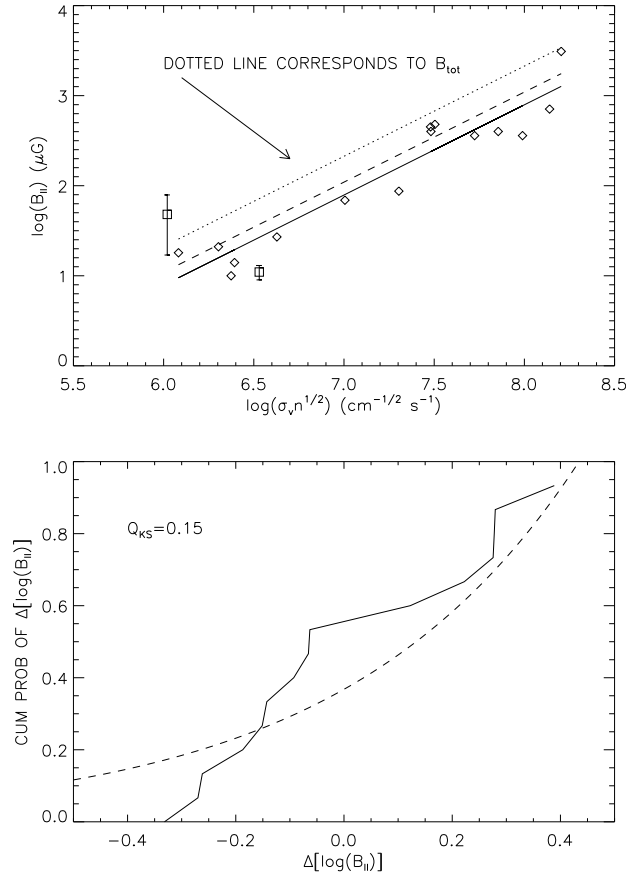


Fig. 14. The **top panel** shows molecular cloud data from Crutcher (1999), together with the least-squares fit by Basu (2000) (solid line), the correction to B_{tot} (dotted line), and the line for $\mu_{\text{intrinsic}} = 1$ (dashed line). The **bottom panel** is the cumulative distribution of the residuals from the fit; the dashed line is the theoretical cumulative distribution from (26).

$\cos \theta$. We expect considerable uncertainty in the volume density n , because it is estimated using a variety of rather imprecise methods. And we also expect some cosmic scatter! The small residuals $\Delta(\log B_{||}) \sim 0.23$ show that this fit has physical meaning.

Basu's result is robust with respect to the addition of new data. The two squares with errorbars in Fig. 14 are new datapoints, published after his analysis. The one with small errorbars is from OH Zeeman splitting in L1544 (Crutcher & Troland 2000). The one with large errorbars is not regarded as a detection (Levin et al. 2001). Both are consistent with Basu's fit. Although

there are additional Zeeman detections in the Bourke et al. (2001) and Troland & Crutcher (2004) surveys, data on ρ for these clouds are not yet available; these will provide an additional test of the robustness of the Basu result.

Basu's result convincingly shows that his model of the molecular clouds, which is slabs in which pressure, gravity, and magnetism all play important roles, is correct. The straightforward interpretation from comparing the solid and dashed lines in Fig. 14 is that the parameter $c_1^{1/2}/\mu_{\text{obs}}$ is close to unity, which implies both that there isn't much variation in density within the slab and also that the mass to flux ratio is close to the critical value.

We can go further by using the statistical discussion of Sect. 3 to relate the observed field to the total one. We consider two results where this extension is relevant.

We now return to Basu's correlation shown in Fig. 14. The scatter of the datapoints is small, and we must ask whether it is consistent with the statistical distribution of Sect. 3.2 for $\Delta \log B_{\parallel}$. In particular, is the scatter too small to be consistent with a random distribution of orientation of magnetic field?

A least squares fit, such as done by Basu, selects the mean value of datapoints with respect to the fitted function. The residuals of the measured points are $\Delta(\log B_{\parallel}) = \log B_{\parallel} - \langle \log B_{\parallel} \rangle$, where $\langle \log B_{\parallel} \rangle$ is the mean of the distribution. As discussed in Sect. 3.2, the mean of $\log(B_{\parallel}/B_{\text{tot}}) = -0.43$. The distribution of the residuals $\Delta \log(B_{\parallel}/B_{\text{tot}})$ should follow

$$\psi \left(\Delta \log \frac{B_{\parallel}}{B_{\text{tot}}} \right) = 0.85 10^{\Delta \log(B_{\parallel}/B_{\text{tot}})} \quad (25)$$

We wish to compare this predicted distribution with the observed one. Such comparisons are best done on the cumulative distribution using the Kolmogorov-Smirnov (K-S) test. The cumulative distribution that corresponds to (25) is

$$\text{cum} \left(\Delta \log \frac{B_{\parallel}}{B_{\text{tot}}} \right) = 0.368 10^{\Delta \log(B_{\parallel}/B_{\text{tot}})} \quad (26)$$

The bottom panel of Fig. 14 shows the cumulative distribution of the residuals as the solid curve together with the predicted one as the dashed curve. The K-S test gives the probability P_{KS} that the two distributions are not dissimilar; here we have $P_{\text{KS}} = 0.15$, which although it seems small does indeed indicate that the distributions are consistent with being identical.

We conclude that Basu's fit to Crutcher's data is statistically consistent with a randomly oriented set of slabs. Being a least squares fit, Basu's result provides a value $\langle \log(B_{\parallel}/B_{\text{tot}}) \rangle = -0.43$, meaning that it gives $B_{\parallel}/B_{\text{tot}} = 0.37$. To obtain B_{tot} from this fit we should raise the fitted line by the factor $1/0.37 = 2.72$ (which is the base of Napierian logarithms e). The dotted line in the top panel of Fig. 14 shows this correction, which a factor 1.9 times higher than the dashed curve, which represents $\mu_{\text{intrinsic}} = 1$.

In (24), this means that the factor $c_1^{1/2}/\mu_{\text{intrinsic}} = 1.9$. Above we corrected Crutcher's observed mass-to-flux ratios to give $\mu_{\text{intrinsic}} \sim 1.1$. If this is accurate, then the molecular clouds are magnetically dominated subcritical slabs with density contrast of ~ 4 . However, the uncertainties are such that a more appropriate summary statement is as follows: the molecular clouds are close to the cusp of being supercritical and have some density structure within the slab.

8.3 Morphology

In the magnetic support model, the dominant magnetic field means field lines should be smooth, without irregular structure. Clouds will be thin disks or oblate spheroids, since thermal pressure provides the only support along field lines. The field lines should be parallel to the minor axes of clouds. Finally, an original morphology with parallel magnetic field lines will be transformed into an hourglass morphology since it is the tension of the bent field lines that provides support. In the turbulent model, the magnetic field will be too weak to resist twisting by the dominant turbulence, and field lines will not be smooth but chaotic, with small-scale irregular structure. No correlation with cloud morphology is expected.

Maps of dust and spectral-line linear polarization and of the Zeeman effect generally show a regular field morphology (e.g., Figs. 8, 9, and 10), and an hourglass morphology is sometimes seen (e.g., Fig. 9; see also Schleuning 1998). A regular field dominating a random field and an hourglass morphology toward cores are predictions of the strong magnetic field model. However, the magnetic field vector projected onto the sky is not observed to be parallel to the minor axes of starless cores as predicted by magnetic support (e.g., Fig. 8). Finally, even though fairly small, the dispersion in polarization position angles is often greater than observational errors (e.g., Fig. 8), implying that turbulence is producing an irregular component to the magnetic field.

9 Magnetic Field Observations, Present and Future

The field is currently in excellent health, with an unbiased survey of absorption lines that provide statistically reliable (if noisy) magnetic field strengths in the CNM, and a host of statistically biased measurements with some instrumental errors in emission regions. There are a number of molecular clouds with measured field strengths or sensitive limits, and study of the field morphology in the plane of the sky from dust and spectral-line linear polarization mapping is rapidly advancing. From all these measurements we conclude that the magnetic energy density is comparable to turbulence, or larger in some regions, and that molecular clouds are well-defined by models that incorporate both gravity and magnetism. These results are hard-won: they require

much telescope time and, for the emission measurements, careful evaluation and correction of instrumental contributions.

What does the future hold? In particular, what can we expect from new instruments?

9.1 H I Zeeman in Absorption

Current Telescopes

The Arecibo Millennium survey, discussed in Sect. 4, has provided much useful statistical quantitative information about magnetic fields in the CNM. It used nearly 1000 hours of Arecibo telescope time to survey 79 sources in H I absorption, of which 40 (plus Cas A from HCRO) had useful sensitivity for Zeeman-splitting analysis. The survey was sensitivity limited. To significantly improve the statistics, one would want, say, four times as many sources. As we go for more sources we inevitably go for weaker sources, so a significant improvement would cost perhaps 10000 hours of Arecibo time. In our opinion, getting such a time block for Zeeman splitting measurements – indeed, for any single scientific project – is unlikely. And using any other telescope, with its necessarily lower sensitivity, takes even longer. Except for special purpose projects, we see no useful future for H I absorption Zeeman splitting measurements using existing telescopes⁵.

The SKA

The Square Kilometer Array (SKA) will have sensitivity about 40 times larger than Arecibo. However, this doesn't mean that the sensitivity-limited results go $40^2 = 1600$ times faster. The reason is that any set of reasonable sources would all be stronger than the SKA's system noise so integration time would be independent of source flux or system sensitivity. In other words, 10 hours on the SKA would provide the same limiting magnetic field strength for both a 100 mJy source and a much stronger 1 Jy source. If a new Millennium survey were performed using 1000 hours of SKA time, then about the same number of sources could be covered as in the original Millennium survey. This would be nice, but would probably not represent a major scientific advance. We conclude that H I Zeeman-splitting absorption line survey work using the SKA is unlikely to prosper.

⁵ This statement applies only to diffuse H I. The excellent set of Zeeman-splitting measurements in H I associated with H II regions and supernova remnants, made with the VLA (e.g., Brogan & Troland 2001), can be extended to many more sources.

9.2 H I in Emission

Current and Future Telescopes

For H I emission, minimizing sidelobes, with their concomitant instrumental contribution to Zeeman splitting, is paramount. This rules out Arecibo (Heiles & Troland 2004). It makes two telescopes very attractive:

1. The Green Bank Telescope. The GBT is totally unique as a single dish because, with its clear aperture, it should have no significant distant sidelobes. While its sidelobes are indeed low, nevertheless we see their effects, both in ordinary H I profiles (Stokes I) and also in Zeeman splitting (Stokes V). We have measured these sidelobes with complete sampling to $\sim 7^\circ$ from beam center and with incomplete sampling out to $\sim 24^\circ$. This larger field shows, surprisingly, that there seems to be little spillover from over-illumination of the secondary. Rather, most of the Stokes V effects come from within the smaller angular field. This is good news, because it means that it might be possible to correct for their instrumental contributions.

We are currently studying the details of these sidelobes and expect to understand them well enough to subtract out their contribution to H I emission Stokes V spectra. The degree to which we can correct the GBT's sidelobes will determine what projects in H I emission are feasible. Projects for which the corrections should be easy include external galaxies other than M 31 (because emission is restricted in angle) and the CNM in the Milky Way (because lines are narrow). Projects for which success should depend more seriously on corrections include M 31 (emission is extended, with large velocity gradients) and the WNM in the Milky Way (lines are weak and broad). Time will tell which projects are feasible.

2. The Allen Telescope Array. The ATA is unique among arrays in having plenty of small baselines, which helps to provide good brightness temperature sensitivity. At the 21-cm line the angular resolution will about ten arcsec and the field of view some $2^\circ.5$; a long integration on one field of view will produce a map with 10^6 pixels. Moreover, the sidelobe properties of synthesis arrays are very well understood, so their effects should be removable with rather good accuracy. This will be an exciting instrument and has the potential of revolutionizing our understanding of magnetic fields in the ISM!

9.3 Molecular Clouds

Current Telescopes

The major telescopes used for Zeeman studies of molecular clouds are the VLA, Arecibo, the IRAM 30-m, and the GBT. Including the recently completed but unpublished survey of OH Zeeman toward dark clouds at Arecibo

by Troland & Crutcher, there are 27 detections toward 81 positions or clouds. Because of the very large amount of telescope time that has been expended in the OH surveys, further advances with single-dish telescopes will probably come from Zeeman detections in CN and other species (excited OH, SO, C₂S, C₂H, ...) that sample high-density gas rather than from additional surveys in H I and the ground-state OH lines. The improvements to the VLA (including especially the new correlator) that will result in the EVLA will improve H I and OH absorption-line Zeeman mapping of clouds.

Current telescopes that have been actively used for mapping polarized dust emission include the CSO, JCMT, and BIMA. The upgrade of the SCUBA array on the JCMT and the combination of the BIMA and OVRO arrays into CARMA will lead to significant improvements in sensitivity that will allow many more clouds to be mapped with higher sensitivity. Similarly, CARMA should extend studies of linearly polarized line emission to additional clouds. And the SMA will complement CARMA with access to higher frequencies, although with a smaller number of antennas.

Future Telescopes

ALMA will very significantly improve the sensitivity available for dust polarization and spectral-line linear polarization observations. With its single-dish and compact array components, very large number of antennas, and high site, ALMA should routinely allow high fidelity polarization mapping over extended areas of molecular clouds. For Zeeman observations of millimeter-wave spectral lines, the improvement in sensitivity will be more modest, but should make possible mapping of B_{\parallel} in (for example) CN in a limited number of clouds.

Although as noted above the SKA will not make it possible to significantly improve the astrophysical results that were obtained from the Millennium Survey, its high sensitivity will greatly increase the surface density of background continuum sources that are strong enough for H I and OH Zeeman-splitting measurements, making it possible to measure and map magnetic field strengths in just about any specific cloud of interest.

It is a pleasure to acknowledge the pleasurable collaborations with many Zeeman-splitting friends over the years, especially Tom Troland. Tim Robshaw was indispensable for the GBT data. Mordecai-Mark MacLow made the important suggestion regarding equipartition of turbulence and magnetism, which we discussed in Sect. 4.5. This work was partially supported by NSF grants AST 02-05810 and AST 04-06987.

References

1. Argon, A. L., Reid, M. J., Menten, K. M.: 2000, ApJS 129, 159

2. Basu, S.: 2000, ApJ 540, L103
3. Batrla, W., Menten, K.M.: 1988, ApJ 329, L117
4. Beck, R.: 2001, Sp. Sci. Rev. 99, 243
5. Beck, R., Shukurov, A., Sokoloff, D., Wielebinski, R.: 2003, A&A 411, 98
6. Berkhuijsen, E. M., Haslam, C. B. T., Salter, C.J.: 1971, A&A 14, 252
7. Boulares, A., Cox, D. P.: 1990, ApJ 365, 544
8. Bourke, T.L., Myers, P.C., Robinson, G., Hyland, A.R.: 2001, ApJ 554, 916
9. Brogan, C. L., Troland, T. H.: 2001, ApJ 560, 821
10. Caswell, J. L.: 2003, MNRAS 341, 551
11. Caswell, J. L.: 2004, MNRAS 352, 101
12. Chandrasekhar, S., Fermi, E.: 1953, ApJ 118, 113
13. Chrysostomou, A., Aitken, D. K., Jenness, T., Davis, C. J., Hough, J. H., Curran, R., Tamura, M.: 2002, AAP 385, 1014
14. Ciolek, G. E., Basu, S.: 2000, ApJ 529, 925
15. Crutcher, R.M., Troland, T.H., Goodman, A.A., Heiles, C., Kazès, I., Myers, P.C.: 1993, ApJ 407, 175
16. Crutcher, R.M., Troland, T.H., Lazareff, B., Paubert, G., Kazès, I.: 1999, ApJ 514, L121
17. Crutcher, R. M.: 1999, ApJ 520, 706
18. Crutcher, R. M., Troland, T. H.: 2000, ApJ 537, L139
19. Crutcher, R. M., Heiles, C., Troland, T.: 2003, in *Turbulence and Magnetic Fields in Astrophysics*, ed. E. Falgarone, T. Passot, Lecture Notes in Physics 614 (Berlin: Springer) p. 155
20. Crutcher, R.M., Nutter, D., Ward-Thompson, D., Kirk, J.M.: 2004, ApJ 600, 279
21. Davies, R.D.: 1974, IAUS 60, 275
22. Davis, L., Greenstein, J. L.: 1951, ApJ 114, 206
23. Draine, B. T.: 2003, ARA&A 41, 241
24. Elmegreen, B.G.: 2000, ApJ 530, 277
25. Fiebig, D., Güsten, R.: 1989, AAP 214, 333
26. Ferrière, K., Mac Low, M.-M., Zweibel, E.: 1991, ApJ 375, 239
27. Fiedler, R. A., Mouschovias, T. Ch.: 1993, ApJ 415, 680
28. Field, G. B.: 1965, ApJ 142, 531
29. Fish, V. L., Reid, M. J., Argon, A. L., Menten, K. M.: 2003, ApJ 596, 328
30. Genzel, R., Downes, D.: 1977, Astron. Astrophys. Suppl. 30, 145
31. Girart, J.M., Crutcher, R.M., Rao, R.: 1999, ApJ 525, L109
32. Goldreich, P., Kylafis, N.D.: 1981, ApJ 243, L75
33. Goodman, A. A., Heiles, C.: 1994, ApJ 424, 208
34. Heiles, C.: 1967, ApJS 15, 97
35. Heiles, C.: 1984, ApJS 55, 585
36. Heiles, C.: 1988, ApJ 324, 321
37. Heiles, C.: 1989, ApJ 336, 808
38. Heiles, C.: 1993, BAAS 25, 829
39. Heiles, C.: 1996a, ApJ 462, 316
40. Heiles, C.: 1996b, ApJ 466, 224
41. Heiles, C.: 1997, ApJS 111, 245
42. Heiles, C.: 1998a, Astrophys. Lett. and Comm. 37, 85
43. Heiles, C.: 1998b, in *The Local Bubble and Beyond*, ed. D. Breitschwerdt, M. J. Freyberg, J. Trümper (Berlin: Springer), p. 229

44. Heiles, C.: 2000a, AJ 119, 923
45. Heiles, C.: 2000b, in *Tetons 4: Galactic Structure, Stars, and the Interstellar Medium*, ed. C. E. Woodward, M. D. Bica, J. M. Shull, ASP Conf. Ser. 231, p. 294
46. Heiles, C., Goodman, A. A., McKee, C. F., Zweibel, E. G.: 1993, in *Protostars and Planets III*, ed. E. H. Levy, J. I. Lunine (Tucson: Univ. of Arizona Press), p. 279
47. Heiles, C., Perillat, P., Nolan, M. et al.: 2001, PASP 113, 1247
48. Heiles, C., Robishaw, T., Troland, T. H.: 2003, Calibrating the GBT at L, C, and X Bands, GBT Commissioning Memo 23, available at www.local.gb.nrao.edu/~rmaddale/GBT/Commissioning/memolist.html
49. Heiles, C., Troland, T. H.: 2003, ApJ 586, 106
50. Heiles, C., Troland, T. H.: 2004, ApJ, in preparation
51. Heitsch, F., Zweibel, E.G., MacLow, M.-M., Li, P.S., Norman, M. L.: 2001, ApJ 561, 800
52. Heyer, M. H., Vrba, F. J., Snell, R. L. et al.: 1987, ApJ 321, 855
53. Hildebrand, R.H.: 1988, Quar. Jour. Roy. Ast. Soc. 29, 327
54. Hildebrand, R. H., Davidson, J. A., Dotson, J. L., Dowell, C. D., Novak, G. F., Vaillancourt, J. E.: 2000, PASP 112, 1215
55. Hildebrand, R. H.: 2002, in *Astrophysical Spectropolarimetry*, Proc. XII Canary Islands Winter School of Astrophysics, ed. J. Trujillo-Bueno, F. Moreno-Insertis, F. Sánchez (Cambridge), p. 265
56. Hildebrand, R.: 2003, New Astronomy Review 47, 1009
57. Jenkins, E. B., Tripp, T. M.: 2001, ApJS 137, 297
58. Kylafis, N. D.: 1983, ApJ 275, 135
59. Lai, S.-P., Girart, J.M., Crutcher, R.M.: 2003, ApJ 598, 392
60. Lazarian, A.: 2003, J. Quant. Spectrosc. Radiat. Trans. 79, 881 (also astro-ph/0208487)
61. Levin, S. M., Langer, W. D., Velusamy, T., Kuiper, T. B. H., Crutcher, R. M.: 2001, ApJ 555, 850
62. MacLow, M., Klessen, R. S., Burkert, A., Smith, M. D.: 1998, Phys. Rev. Lett. 80, 2754
63. MacLow, M., Klessen, R. S.: 2004, Rev. Mod. Phys. 76, 125
64. Matthews, B.C., Wilson, C.D., Fiege, J.D.: 2001, ApJ 562, 400
65. McKee, C. F., Ostriker, J. P.: 1977, ApJ 218, 148
66. Mestel, L. & Spitzer, L., Jr.: 1956, MNRAS 116, 505
67. Mouschovias, T. Ch.: 1976, ApJ 206, 753
68. Mouschovias, T.Ch., Ciolek, G.E. (1999) in *The Origin of Stars and Planetary Systems*, eds. C. J. Lada, N. D. Kylafis, Kluwer, p. 305.
69. Myers, P. C., Goodman, A. A., Güsten, R., Heiles, C.: 1995, ApJ 442, 177
70. Nakano, T., Nakamura, T.: 1978, PASJ 30, 671
71. Norman, C., Ikeuchi, S.: 1989, ApJ 345, 372
72. Norris, R.P., Booth, R.S., Diamond, P.J., Porter, N.D.: 1982, MNRAS 201, 191
73. Ostriker, E.C., Stone, J.M., Gammie, C.F.: 2001, ApJ 546, 980
74. Padoan, P., Goodman, A., Draine, B.T., Juvela, M., Nordlund, Å., Röngrvaldsson, Ö.E.: 2001, ApJ 559, 1005
75. Pereyra, A., Magalhaes, A. M.: 2004, ApJ 603, 584
76. Purcell, E. M.: 1979, ApJ 231, 404
77. Purcell, E. M., Spitzer, L.: 1971, ApJ 167, 31

78. Roberts, D. A., Crutcher, R. M., Troland, T. H.: 1995, ApJ 442, 208
79. Sarma, A. P., Troland, T. H., Romney, J. D.: 2001, ApJ 554, L217
80. Sarma, A. P., Troland, T. H., Crutcher, R. M., Roberts, D. A.: 2002, ApJ 580, 928
81. Schleuning, D.A.: 1998, ApJ 493, 811
82. Schneider, N., Simon, R., Kramer, C., Stutzki, J., Bontemps, S.: 2002, AAp 384, 225
83. Schwarz, U. J., Troland, T. H., Albinson, J. S., Bregman, J. D., Goss, W. M., Heiles, C.: 1986, ApJ 301, 320
84. Slavin, J. D., Cox, D. P.: 1992, ApJ 392, 131
85. Spitzer, L., Jr.: 1942, ApJ 95, 329
86. Tomisaka, K.: 1990, ApJ 361, L5
87. Troland, T. H., Heiles, C.: 1982, ApJ 372, 179
88. Troland, T. H., Crutcher, R. M., Heiles, C.: 1985, ApJ 298, 808
89. Troland, T.H., Heiles, C.: 1986, ApJ 301, 339
90. Troland, T.H. (2004) in *The Magnetized Interstellar Medium*, eds. B. Uyaniker, W. Reich, R. Wielebinski, Copernicus GmbH, Katlenburg-Lindau., p. 105-114
91. Troland, T.H., Crutcher, R.M.: 2004, ApJ , to be submitted
92. Trumpler, R. J., Weaver, H. F.: 1953, *Statistical Astronomy* (New York: Dover)
93. Verschuur, G. L.: 1969, ApJ 156, 861
94. Verschuur, G. L.: 1974, in *Galactic and Extra-Galactic Radio Astronomy*, ed. G. L. Verschuur, K. I. Kellermann (New York:: Springer), p. 179
95. Verschuur, G. L.: 1989, ApJ 339, 163
96. Verschuur, G. L.: 1993, BAAS 25, 1466
97. Verschuur, G. L.: 1995a, ApJ 451, 624
98. Verschuur, G. L.: 1995b, ApJ 451, 645
99. Vrba, F. J., Strom, S. E., Strom, K. M.: 1976, AJ 81, 958
100. Wolf, S., Launhardt, R., Henning, T.: 2003, ApJ 592, 233
101. Wolfire, M. G., McKee, C. F., Hollenbach, D., Tielens, A. G. G. M.: 2003, ApJ 587, 278
102. Wolleben, M., Reich, W. (2004) in *The Magnetized Interstellar Medium*, eds. B. Uyaniker, W. Reich, R. Wielebinski, Copernicus GmbH, Katlenburg-Lindau., p. 99-104
103. Woltjer, L.: 1967, in *Radio Astronomy and the Galactic System*, IAU Symp. 31, ed. H. van Woerden (London: Academic Press), p. 479
104. Woody, D.P., Scott, S.L., Scoville, N.Z., Mundy, L.G., Sargent, A.I., Padin, S., Tinney, C.G., Wilson, C.D.: 1989, ApJ 337, L41